PNAS RESEARCH ARTICLE | APPLIED PHYSICAL SCIENCES

Geometric control of topological dynamics in a singing saw

Suraj Shankar[a,1], Petur Bryde[b,1], and L. Mahadevan[a,b,c,2]

Edited by Vincenzo Vitelli, University of Chicago, Chicago, IL; received September 19, 2021; accepted March 3, 2022, by Editorial Board Member Paul Chaikin

The common handsaw can be converted into a bowed musical instrument capable of producing exquisitely sustained notes when its blade is appropriately bent. Acoustic modes localized at an inflection point are known to underlie the saw's sonorous quality, yet the origin of localization has remained mysterious. Here we uncover a topological basis for the existence of localized modes that relies on and is protected by spatial curvature. By combining experimental demonstrations, theory, and computation, we show how spatial variations in blade curvature control the localization of these trapped states, allowing the saw to function as a geometrically tunable high-quality oscillator. Our work establishes an unexpected connection between the dynamics of thin shells and topological insulators and offers a robust principle to design high-quality resonators across scales, from macroscopic instruments to nanoscale devices, simply through geometry.

musical acoustics | topological insulators | thin elastic shells

Significance

The ability to sustain notes or vibrations underlies the design of most acoustic devices, ranging from musical instruments to nanomechanical resonators. Inspired by the singing saw that acquires its musical quality from its blade being unusually bent, we ask how geometry can be used to trap and insulate acoustic modes from dissipative decay in a continuum elastic medium. By using experiments and theoretical and numerical analysis, we demonstrate that spatially varying curvature in a thin shell can localize topologically protected modes at inflection lines, akin to exotic edge states in topological insulators. A key feature is the ability to geometrically control both spatial localization and the dynamics of oscillations in thin shells. Our work uncovers an unusual mechanism for designing robust, yet reconfigurable, high-quality resonators across scales.

Musical instruments, even those made from everyday objects such as sticks, saws, pans, and bowls (1), must have the ability to create sustained notes for them to be effective. While this ability is often built into the design of the instruments, the musical saw, used to make music across the world for over a century and a half (2), is unusual in that it is just a carpenter's saw but held in an unconventional manner to allow it to sing. When a saw (Fig. 1*A*) is either bowed or struck by a mallet, it produces a sustained sound that mimics a "soprano's lyric trill" (3). Importantly, for such a note to be produced, the blade cannot be flat or bent into a J shape (Fig. 1*B*) but must be bent into an S shape (Fig. 1*C*). This geometric transformation allows the saw to sing and is well known to musicians who describe the presence of a "sweet spot," i.e., the inflection curve in the S-shaped blade; bowing near it produces the clearest notes, while bowing far from it causes the saw to fall silent (3). Early works (4, 5), including notably Scott and Woodhouse (6), attempted to understand this peculiar feature by analyzing the linearized vibrational modes of a thin elastic shell (7, 8). Through a simplified asymptotic analysis, they showed that a localized vibrational eigenmode emerges at an inflection point in a shell with spatially varying curvature and is responsible for the musicality of the saw. Recent works have reproduced this result using numerical simulations (9, 10), but a deeper understanding of the origin of localization has remained elusive.

A simple demonstration of playing the saw quickly reveals the robustness of its musical quality to imperfections in the saw, irregularities in its shape, and the precise details of how the blade is flexed. Fig. 1*D* shows a time trace and spectrogram of the saw clamped in either a J shape or an S shape (Fig. 1 *B* and *C*) when struck or bowed near the sweet spot. The dull and short-lived sound (Audio 1) associated with the J shape might be contrasted with the nearly pure tone (≈595 Hz) lasting several seconds (Audio 2) when the saw is bowed while shaped like an S. While the pitch can be varied by changing the curvature of the saw, the sustained quality of the note is largely indifferent to the manner of excitation and the specific nature of the clamps, as long as the inflection point is present.

The lack of sensitivity to these details suggests a topological origin for the localized mode responsible for the saw's striking sonority. That topology can have implications for band structures and the presence of edge conducting states even when the bulk is insulating was originally explored in electronic aspects of condensed matter to explain the quantization of the Hall conductance (11) and led to the prediction of topological insulators (12, 13). More recently, similar ideas have been used to understand the topological properties of mechanical excitations, e.g., acoustic and floppy modes in discrete periodic lattices (14–17), in continuum elasticity (18–21), in fluid dynamics in geophysical and active matter systems (22–25), etc. In many of the aforementioned systems, the breaking of time-reversal symmetry leads to the appearance of topologically protected modes. Alternately, in the absence of driven or active elements, spatial symmetries of a unit cell can also be used to achieve topological modes via acoustic analogs of the quantum spin or valley Hall effect (17, 26–29), although these examples rely on carefully engineered periodic lattices. Here we expand the use of topological ideas to continuum shells and show that

Author contributions: L.M. conceived research; S.S., P.B., and L.M. designed research; S.S. and P.B. performed research; S.S., P.B., and L.M. contributed new analytic tools; S.S., P.B., and L.M. analyzed data; and S.S., P.B., and L.M. wrote the paper.

The authors declare no competing interest.

This article is a PNAS Direct Submission. V.V. is a guest editor invited by the Editorial Board.

[1]S.S. and P.B. contributed equally to this work.

[2]To whom correspondence may be addressed. Email: lmahadev@g.harvard.edu.

This article contains supporting information online at https://www.pnas.org/lookup/suppl/doi:10.1073/pnas.2117241119/-/DCSupplemental.

Published April 21, 2022.

underlying the time-reversible Newtonian dynamics of the singing saw is a topological invariant that characterizes the propagation of waves in thin shells, arising from the breaking of up–down inversion symmetry by curvature.

Results

Continuum Model of Thin Shell Dynamics. The saw is modeled as a very thin rectangular elastic shell (thickness $h \ll W < L$, where W, L are the width and length of the strip) made of a material with Young's modulus Y, Poisson ratio ν, and density ρ (Fig. 1*E*). Its geometry is characterized by a spatially varying curvature tensor (second fundamental form) $\mathbf{b}(\mathbf{x})$, where $\mathbf{x} = (x, y)$ is the spatial coordinate in the plane. As the saw is bent only along the (long) x axis, $b_{xx}(x) \equiv b(x)$ is the sole nonvanishing curvature. To describe its dynamical response, we take advantage of its slenderness and treat the saw as a thin elastic shell that can be bent, stretched, sheared, and twisted. Before moving to a computational model that accounts for these modes of deformation as well as real boundary conditions, to gain some insight into the problem and expose the topological nature of elastic waves, it is instructive to instead consider a simplified description valid for shallow shells with slowly varying curvature.

In a thin shallow shell ($h|b_{ij}| \ll 1$), as bending is energetically cheaper than stretching (30), shear becomes negligible ($\mathbf{Q} \approx \mathbf{0}$; Fig. 1*E*), and in-plane deformations propagate much more rapidly (at the speed of sound $c = \sqrt{Y/\rho}$) so that the depth-averaged stresses can be assumed to equilibrated, i.e., $\partial_j \sigma_{ij} = 0$ (6, 31). In this limit, using the solution of these equations in terms of the Airy stress function χ ($\sigma_{ij} = \mathcal{P}_{ij}\nabla^2\chi$, where $\mathcal{P}_{ij} = \delta_{ij} - \partial_i\partial_j/\nabla^2$ is a projection operator; *SI Appendix*, section 3), the in-plane geometric compatibility relation and the linearized dynamical equations for transverse motions can be written as (7, 32)

$$\frac{1}{Yh}\nabla^4\chi = -\mathcal{P}_{ij}\nabla^2(b_{ij}f), \qquad [1]$$

$$\rho h\partial_t^2 f = -\kappa\nabla^4 f + b_{ij}\mathcal{P}_{ij}\nabla^2\chi. \qquad [2]$$

Here f is the out-of-plane deflection of the shell (Fig. 1*E*) and the bending rigidity $\kappa = Yh^3/[12(1-\nu^2)]$. Crucially, in-plane and flexural (out-of-plane) modes remain geometrically coupled in the presence of curvature even in the linearized setting (Eqs. 1 and 2). For a shell bent with constant curvature along the x axis, i.e., a section of a uniform cylinder, $b(x) = b_0$ is a constant. In the bulk of the system, disregarding boundaries, we can Fourier transform Eqs. **1** and **2** using the solution ansatz $f = f_{\mathbf{q}}e^{-i\omega t + i\mathbf{q}\cdot\mathbf{x}}$ to obtain the dispersion relation for flexural waves to be $\omega_\pm(\mathbf{q}) = \pm\sqrt{(\kappa/\rho h)q^4 + c^2 b_0^2 (q_y/q)^4}$ (Fig. 2*A*), where $q = |\mathbf{q}|$. When $q_y = 0$, i.e., the sheet is undeformed in the transverse direction, it remains developable (with generators that run parallel to the y direction), and the bending waves are gapless, i.e., $\omega \to 0$ as $q \to 0$. However, when $q_y \neq 0$, a finite frequency gap $\sim c|b_0|$ (in addition to finite q_y corrections) controlled by the speed of sound and the curvature of the shell emerges as $q \to 0$ (Fig. 2*A*). Intuitively, this arises due to the geometric coupling between bending and stretching deformations in a curved shell which leads to an effective stiffening that forbids wave propagation below a frequency threshold. Similar spectral gaps appear in curved filaments and doubly curved shells as well (31, 33).

For the S-shaped saw, curvature scales of $b \sim 0.4$ to $0.8\ \mathrm{m}^{-1}$ are easily achievable (as in Fig. 1 *B* and *C*), while the typical sound speed in steel is $c \sim 5$ to 6×10^3 m/s so that the frequency gap is of order 2 to 5 kHz. Comparing these estimates to the spectrogram in Fig. 1*D* (further quantified in Fig. 3) suggests that the localized mode excited upon bowing the S-shaped saw (Fig. 1*C*) lies within the frequency gap. The J-shaped saw (Fig. 1*B*) also vibrates at low frequencies (compared to the gap) when struck, presumably through the $q_y = 0$ branch of delocalized flexural modes, although higher frequencies above the band gap can be excited by careful bowing (*SI Appendix*, Fig. S1 *A* and *B*).

Curvature-Induced $\mathbb{Z}_2$ Topological Invariant. To unveil the topological structure of the vibration spectrum of the saw, we cast the second-order dynamical equations (Eqs. **1** and **2**) in terms of first-order equations by taking the square root of the dynamical matrix (14, 34). Focusing on the flexural modes alone, we obtain a Schrödinger-like equation for the transverse deflections of a shallow shell (*SI Appendix*, section 3),

$$\frac{i}{c}\partial_t\Psi = \mathcal{H}\Psi, \quad \mathcal{H} = \begin{pmatrix} 0 & \mathcal{D}^\dagger \\ \mathcal{D} & 0 \end{pmatrix}, \qquad [3]$$

where $\Psi = (c\mathcal{D}^\dagger f,\ i\partial_t f)$ and $\mathcal{D} = i\sqrt{\kappa/Yh}\nabla^2 + b_{ij}\mathcal{P}_{ij}$ and $\dagger$ represents the conjugate transpose. The eigenvalues of the effective Hamiltonian $\mathcal{H}$ are given by the previously derived ($\omega_\pm(\mathbf{q})$), and its complex eigenvectors $\Psi_\pm(\mathbf{q})$ encode the topology of the band structure. The singularities in the arbitrary phase of the eigenvectors signals nontrivial band topology. To understand the phase of eigenvectors along the saw's long direction, we can consider fixing the transverse wave vector $q_y \neq 0$, leading to an effective one-dimensional (1D) system along the x axis. Then the obstruction to continuously define the phase of the eigenvectors at every q_x in Fourier space while respecting all the symmetries of the problem is quantified by the 1D Berry connection $\mathcal{A}(q_x) = i\sum_{n=\pm}\Psi_n(q_x)^\dagger\partial_{q_x}\Psi_n(q_x)$ (the q_y dependence is suppressed) (35, 36). However, what are the symmetries of our elastodynamic system?

One important symmetry is that imposed by classical time-reversal invariance in a passive, reciprocal material ($\mathcal{C} : x \to x$, $t \to -t$, $\Psi \to \Psi^*$; *SI Appendix*, section 3), which maps forward moving waves into backward moving ones and guarantees that eigenmodes appear in complex-conjugate pairs (34). A second symmetry special to the saw is an emergent spatial reflection symmetry in the local tangent plane ($\Pi : x \to -x$, $t \to t$, $\Psi \to \Psi$; *SI Appendix*, section 3), which originates from the uniaxial nature of the prescribed curvature along the x axis and the insensitivity of bending to the orientation of the local tangent plane, a symmetry that is inherited from 3D rotational invariance. The latter is easily seen by noting that the bending energy only involves an even number of gradients via $\nabla^2 f$. Upon simultaneously enforcing both dynamical and spatial symmetries, a new topological obstruction posed by curvature emerges and is quantified by a $\mathbf{Z}_2$ index (*SI Appendix*, section 3),

$$(-1)^\nu = \exp\left[i\int_0^\infty \mathrm{d}q_x\,\mathcal{A}(q_x)\right]\frac{\mathrm{Pf}[\mathbf{W}(0)]}{\mathrm{Pf}[\mathbf{W}(\infty)]}, \qquad [4]$$

similar to topological insulators with crystalline symmetries (37–39). $\mathrm{Pf}[\mathbf{W}]$ denotes the Pfaffian of the antisymmetric overlap matrix $W_{ij}(q_x) = \Psi_i(q_x)^\dagger\mathcal{C}\Pi\Psi_j(q_x)$ $(i, j = \pm)$. We note that unlike the mechanical Su–Schrieffer–Heeger chain (14) that exhibits a topological polarization in 1D, the emergent tangent-plane spatial reflection symmetry in our problem forces this polarization to vanish (*SI Appendix*, section 3).

As we work in the continuum, only differences in the topological invariant are well defined independent of microscopic details. Across an interface at which curvature changes sign, i.e., a curvature domain wall, the jump in the topological invariant is given by

$$(-1)^{\Delta\nu} = \mathrm{sgn}(b_< b_>), \qquad [5]$$

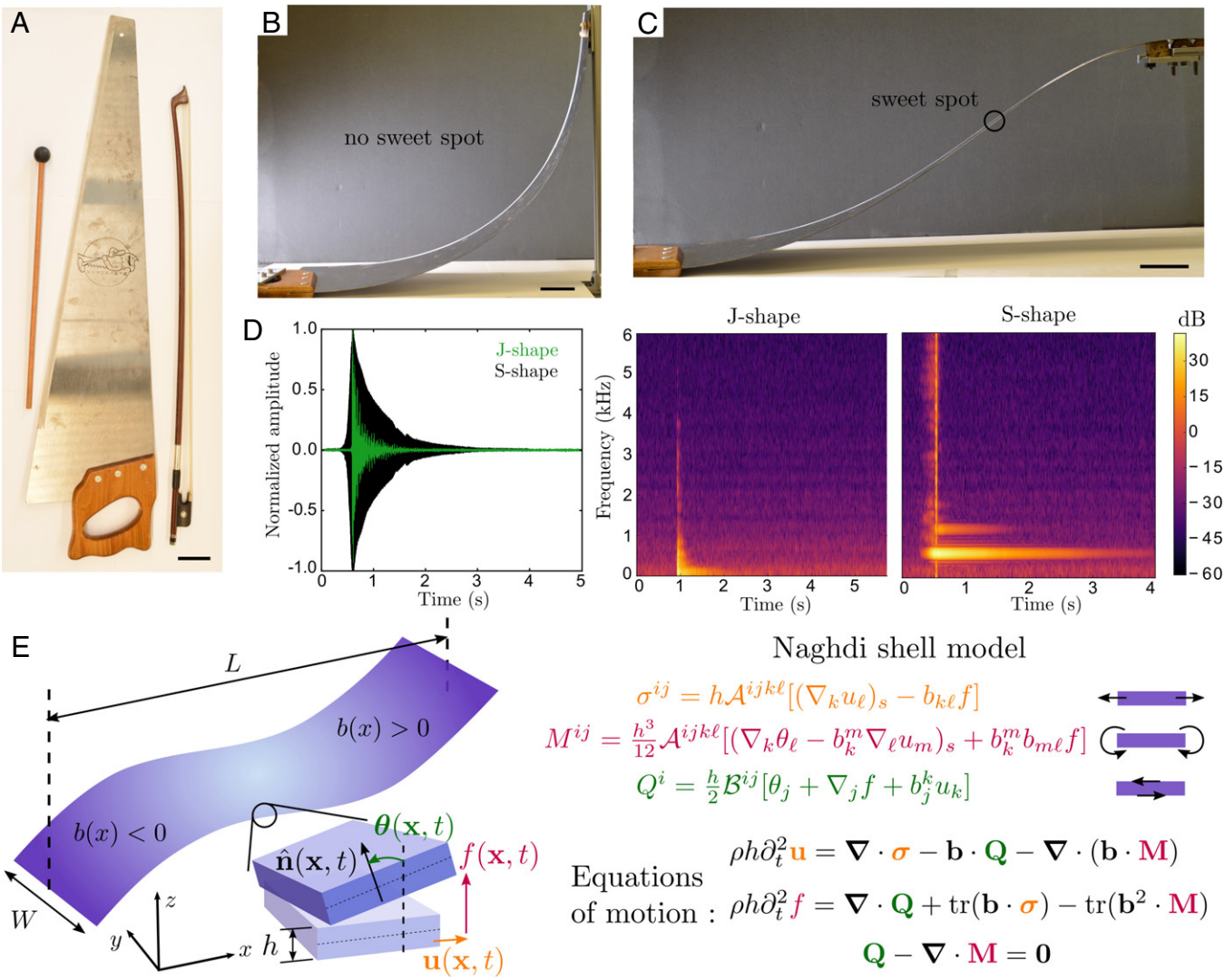

Fig. 1. The musical saw and its mathematical model. (*A*) A violin bow and mallet placed alongside the saw. We clamp the saw in two configurations: (*B*) a J shape and (*C*) an S shape, which is required to play music. The primary distinction between the two is that *C* has an inflection point (the sweet spot) in its profile, while *B* has curvature of constant sign. (Scale bar, 5 cm.) (*D*) (*Left*) Time series of the normalized audio signal when the saw in *B* is struck (green) and when the saw in *C* is bowed (black). (*Middle* and *Right*) The corresponding spectrograms for both the J shape (*B*) and the S shape (*C*). The signal decays rapidly for the J shape with a wider spread in frequency, while for the S shape, a single dominant note with $\omega \approx 595$ Hz survives the ringdown of the blade lasting several seconds. (*E*) A schematic of a blade of length *L*, width *W*, and thickness *h* is sketched with a uniaxial curvature profile $b_{xx}(x) \equiv b(x)$ that changes sign along the *x* axis as in *B*. The saw can be modeled as an elastic shell whose deformations include an in-plane displacement $\mathbf{u}$, a midsurface deflection f normal to the shell, and a rotation $\boldsymbol{\theta}$ of the local normal $\hat{\mathbf{n}}$ as degrees of freedom [$\mathbf{x} = (x, y)$ is the spatial coordinate]. Elastic tensors $\mathcal{A}^{ijk\ell}$ and $\mathcal{B}^{ij}$ enter the constitutive equations (subscript s denotes symmetrization) for the in-plane stress ($\boldsymbol{\sigma}$), bending moment ($\mathbf{M}$), and transverse shear ($\mathbf{Q}$) (*SI Appendix*, section 2). Derivatives are interpreted as covariant, and index manipulations employ the reference metric of the shell (*SI Appendix*, section 2). The Kirchhoff limit for a shallow shell simplifies the dynamics to $\nabla \cdot \boldsymbol{\sigma} = \mathbf{0}$, $\rho h \partial_t^2 f = \nabla\nabla : \mathbf{M} + \mathrm{tr}(\mathbf{b} \cdot \boldsymbol{\sigma})$, along with $\boldsymbol{\theta} = -\nabla f - \mathbf{b} \cdot \mathbf{u}$ (*SI Appendix*, sections 2 and 3).

where $b_<$ and $b_>$ are the curvature on either side of the interface (*SI Appendix*, section 3). This expression directly demonstrates that the two oppositely curved sections of the saw behave as topologically nontrivial bulk systems, with a $\Delta\nu = 1$, that meet at the inflection line that functions as an internal edge. As a result, nontrivial band topology underlies the emergence of the localized midgap mode, endowing it with robustness against details of the curvature profile and weakly nonlinear deformations (*SI Appendix*, section 3).

Numerical Mode Structure and Localization. We test these predictions by numerically computing the eigenmodes of a finite elastic strip of length $L = 1$ m, width $W = 0.25$ m, and thickness $h = 10^{-3}$ m. For our shell model, we move away from the Kirchhoff model for shells and account for the kinematics associated with shear in addition to those associated with bending and stretching, as they effectively reduce the numerical ill-conditioning commonly seen in high-order continuum theories for slender plates and shells while allowing for numerical methods that require less smoothness and are easier to implement (*SI Appendix*); together, these allow for better computational accuracy. This framework forms the basis for the Naghdi shell model (40) (see *SI Appendix*, section 2, for details) and accounts for an in-plane displacement vector along the midsurface $\mathbf{u}(\mathbf{x}, t)$, an out-of-plane deflection $f(\mathbf{x}, t)$ normal to the shell, and an additional rotation $\boldsymbol{\theta}(\mathbf{x}, t)$ of the local normal itself (Fig. 1*E*). These modes of deformations lead to depth-averaged stress resultants associated with stretching ($\boldsymbol{\sigma}$), bending ($\mathbf{M}$), and shear ($\mathbf{Q}$) as shown in Fig. 1*E*. The resulting covariant nonlinear shell theory along with inertial Newtonian dynamics provides an accurate and computationally tractable description of the elastodynamics of thin shells (Fig. 1*E* and *SI Appendix*, section 2). To highlight the topological robustness of our results, in our calculations we vary both the boundary conditions and curvature profiles imposed on the saw.

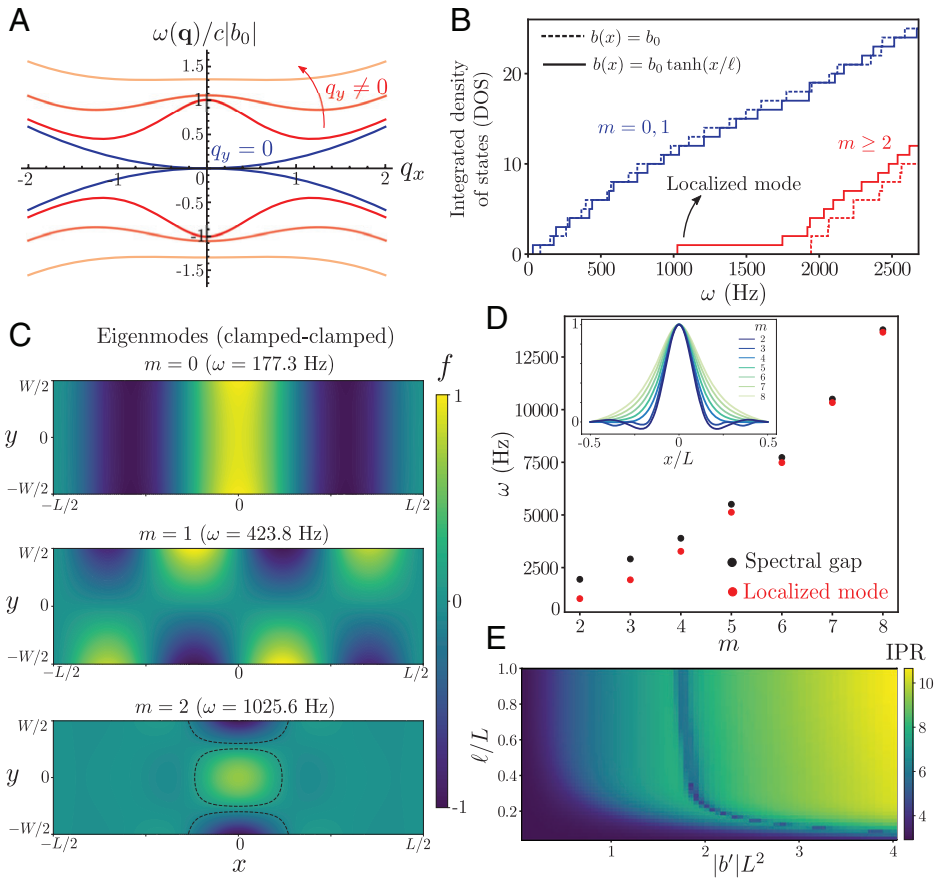

Fig. 2. Eigenmodes, band structure, and topological localization. (*A*) Analytical dispersion relation computed for an infinitely long strip with constant curvature along the *x* axis ($h|b_0| = 5 \times 10^{-5}$, $\nu = 1/3$). The blue curves correspond to the $q_y = 0$ gapless modes, and the red curves with $q_y \neq 0$ have a finite frequency gap. (*B*) Numerically computed integrated density of states for a finite curved strip ($b_0 L = 0.5$, $\ell/L = 0.1$, $L = 1$ m) with clamped–clamped boundary conditions. Developable eigenmodes (blue; labeled by discrete mode numbers $m = 0, 1$, akin to $q_y = 0$ in the continuum) are gapless for both constant curvature (dashed) and the sigmoid profile (solid). Higher modes (red; $m \geq 2$) exhibit a finite gap ∼2 kHz for constant curvature (dashed), while the sigmoid profile features a localized mode ($\omega \sim 1$ kHz) at the inflection point within the bulk band gap. (*C*) Numerical eigenmodes for the sigmoid profile with the local normalized deflection *f* plotted (dashed lines are 10% isocontours). Low-frequency delocalized states with $m = 0$ (*Top*), $m = 1$ (*Middle,*) and the first localized mode with $m = 2$ (*Bottom*). (*D*) Frequency of the localized modes (*Inset* shows normalized deflection at $y = W/2$ along *x*) and corresponding spectral gap for increasing transverse mode number $m \geq 2$. (*E*) Inverse participation ratio of the first localized mode for a piecewise linear curvature profile, plotted against the curvature gradient b' and the length scale of curvature variation ℓ.

In Fig. 2*B*, the distribution of eigenmodes as a function of frequency is shown in the integrated density of states for a constant curvature shell, $b(x) = b_0$ (dashed lines), and an S-shaped shell with a smooth curvature profile $b(x) = b_0 \tanh(x/\ell)$ (solid lines) that varies over a width ℓ near the inflection point at $x = 0$ (i.e., a curvature domain wall). In both cases, the ends of the strip are kept clamped, and the spectra are calculated using an open-source code based on the finite element method (41, 42). As the curvature of the S shape approaches a constant $\pm b_0$ far from the origin, the bulk spectral gap and delocalized modes match that of the constant curvature case. Flexural modes that vary at most linearly in the *y* direction* (labeled by discrete mode numbers $m = 0, 1$ due to the lack of translational invariance) correspond to linearized isometries; they delocalize over the entire ribbon (Fig. 2 *C*, *Top* and *Middle*) and populate states all the way to zero frequency, i.e., with a gapless spectrum. This is true for both constant curvature (dashed blue line, Fig. 2*B*) and the S-shaped shell (solid blue line, Fig. 2*B*) as these bulk modes are unaffected by curvature. In contrast, all other modes that bend in both directions ($m \geq 2$) are generically gapped for a constant curvature profile (dashed red line, Fig. 2*B*) as expected. However, for the S shape, in addition to the gapped bulk modes, a new mode appears within the spectral gap (solid red line, Fig. 2*B*). This midgap state (shown here for $m = 2$) is a localized mode that is trapped in the neighborhood of the inflection line (Fig. 2 *C*, *Bottom*). For increasing mode number $m \geq 2$, similar topological modes appear within the bulk bandgap, with growing localization lengths (Fig. 2 *D*, *Inset*) and higher frequencies (Fig. 2*D*), as predicted analytically (*SI Appendix*, section 3). Qualitatively, the presence of an inflection line in the S-shaped saw makes it geometrically soft there; the generators of cylindrical modes are now along the length of the saw, and the curved regions on either side that are geometrically stiff serve to insulate the soft internal edge from the real clamped edges.

Of particular note is that the localized modes, unlike the extended states, are virtually unaffected by the boundaries and the conditions there (see *SI Appendix*, Fig. S2*A*, for eigenmodes in a strip with asymmetric boundary conditions where the left edge is clamped and the right edge is free). Spatial gradients in curvature, however, do impact the extent of localization. We demonstrate this using a piecewise continuous curvature profile that has a constant linear gradient b' over a length ℓ across the origin and adopts a constant curvature outside this region. By varying both the curvature gradient b' and the length scale ℓ, we can tune the localization of the lowest topological mode (same as Fig. 2 *C*, *Bottom*), quantified by the inverse participation ratio $\mathrm{IPR} = \int \mathrm{d}\mathbf{x}|f(\mathbf{x})|^4 / (\int \mathrm{d}\mathbf{x}|f(\mathbf{x})|^2)^2$ (Fig. 2*E*). Strong localization (high

*Eigenmodes in a finite saw need to vary at least quadratically in *y* (i.e., $m \geq 2$) in order to couple bending and stretching deformations in the shell.

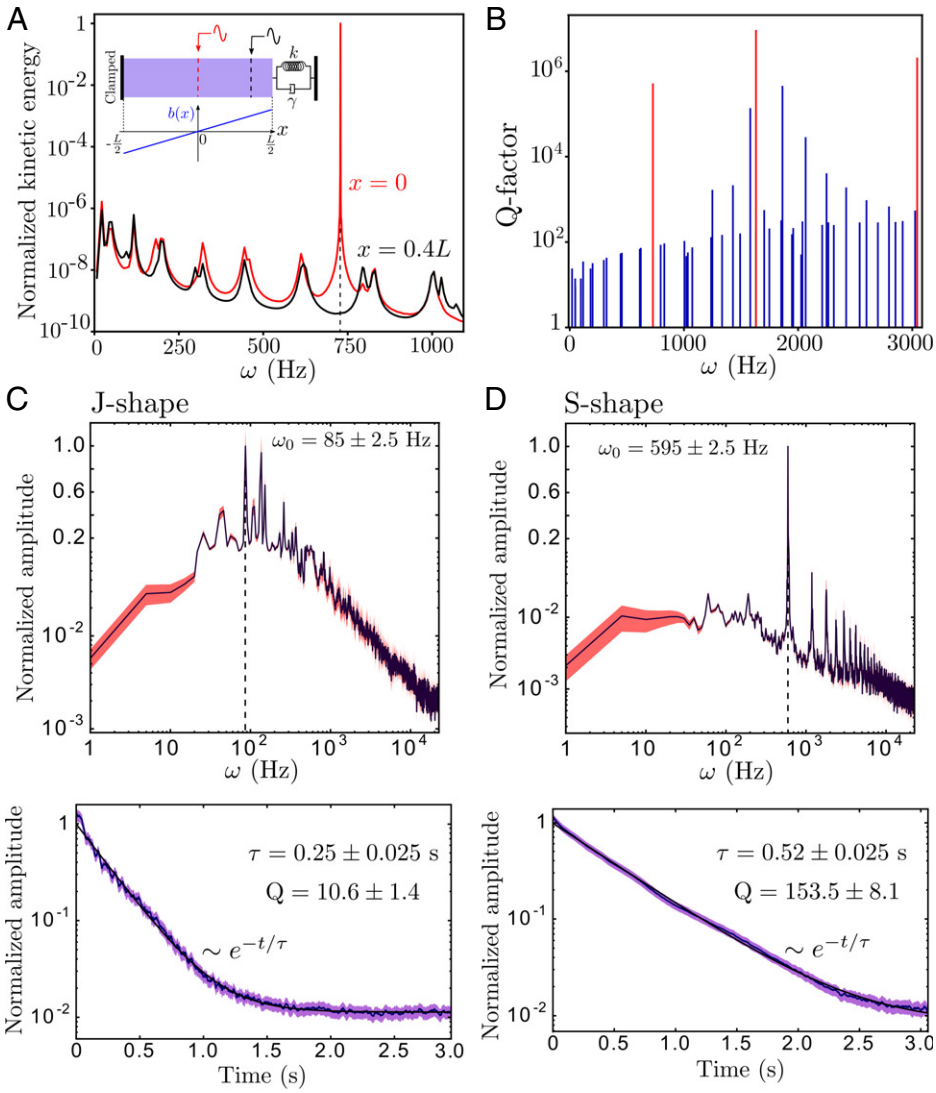

Fig. 3. Dissipative dynamics and high-quality oscillators. (*A*) Resonance curves for a shell with a linear curvature profile (*Inset*) periodically driven at the inflection point ($x = 0$; red) and away from it ($x = 0.4L$; black) for varying frequency ($\omega \approx 740$ Hz corresponds to the first localized mode). (*B*) Numerically computed Q factor shows dramatic enhancement at localized mode frequencies (red) over delocalized modes (blue). (*C* and *D*) Experimental measurement of Q factor (see *SI Appendix*, section 1 for details) for the musical saw in a (*C*) J shape (Fig. 1*B*) and (*D*) S shape (Fig. 1*C*). (*Top*) Note the normalized Fourier spectrum amplitude is on a log scale below 0.1 and linear above, with the peak frequency marked as ω_0. (*Bottom*) The average signal decay (blue curve) is fit to a single decaying exponential (black curve). The shaded region is the SE in both *C* and *D*.

IPR) is quickly achieved for sharp gradients in curvature (IPR $\propto \sqrt{|b'|/h}$; *SI Appendix*, section 3) as long as the length scale of curvature variation is not too small ($\ell/L \geq 0.1$, Fig. 2*E*), corresponding to a diffuse domain wall. In the opposite limit of $\ell \to 0$ for $b'\ell = b_0$ fixed, i.e., a sharp domain wall with a discontinuous curvature profile $b(x) = b_0\,\mathrm{sgn}(x)$, strong localization persists (*SI Appendix*, Fig. S3), consistent with our topological prediction and demonstrating the ease of geometric control of localization.

Geometrically Tunable High-Quality Oscillators. The boundary insensitivity of topologically localized modes has important dynamic consequences that can be harnessed to produce high-quality resonators. The primary mode of dissipation in the saw, as in nanoelectromechanical devices (43), is through substrate or anchoring losses at the boundary. Internal dissipation mechanisms (from, e.g., plasticity, thermoelastic effects, and radiation losses), although present, are considerably weaker and neglected here. To model dissipative dynamics, we retain clamped boundary conditions on the left end and augment the right boundary to include a restoring spring (k) and dissipative friction (γ) for both the in-plane forces and bending moments (Fig. 3 *A*, *Inset*, and *SI Appendix*, section 2). Informed by Fig. 2*E*, we choose a linear curvature profile spanning the entire length of the shell to obtain a strongly localized mode. Upon driving the shell into steady oscillations, with a periodic point force applied at the inflection point ($x = 0$; Fig. 3*A*, red curve), we see an extremely sharp resonance peak right at the frequency of the first localized mode (Fig. 3*A*). In contrast, when the shell is driven closer to the boundary ($x = 0.4L$; Fig. 3*A*, black curve), the response is at least six orders of magnitude weaker as the localized mode is not excited and only the delocalized modes contribute. Localization hence protects the mode from dissipative decay, unlike extended states that dampen rapidly through the boundaries. We further quantify this using a Q factor computed from undriven relaxation of the shell initialized in a given eigenmode (*SI Appendix*, section 2). Ultrahigh values of Q $\approx 10^5$ to 10^6 are easily attained when a localized mode is excited (Fig. 3*B*, red), well over the Q factor of all other modes (Fig. 3*B*, blue). Similar results are obtained for other curvature profiles as well, such as a sigmoid curve (*SI Appendix*, Fig. S2*B*).

To compare these computational results with experiments, we perform ringdown measurements on a musical saw (see *SI Appendix*, section 1, for details) clamped in both the J shape (Fig. 1*B*) and the S shape (Fig. 1*C*). As indicated by Eq. **5**, the key distinguishing feature of the S-shaped saw (compared to the J shape) is the presence of an inflection line (curvature domain wall) that engenders a well-localized domain wall mode capable of sustaining long-lived oscillations. The normalized Fourier spectra and exponential decay (τ) of the signal envelope are shown in Fig. 3*C* (J shape) and Fig. 3*D* (S shape) with the dominant frequency (ω_0) marked. We find a factor $\sim$15 enhancement in the Q factor ($Q = \omega_0\tau/2$) for the S-shaped saw ($Q \approx 150$; Fig. 3 *D*, *Left*) over the J shape ($Q \approx 10$; Fig. 3 *C*, *Left*). We emphasize that this significant quality factor improvement, although not as dramatic as the numerically computed Q factors (Fig. 3*B*), is still striking given the initial impulse (mallet strike for J shape and bow for S shape; see *SI Appendix*, Fig. S1, for other cases) excites an uncontrolled range of frequencies and other sources of energy loss including internal damping are presumably also present.

Discussion and Conclusion

Our combination of analysis, finite element simulations and experiments has demonstrated that a saw sings because its curvature generates a frequency gap in the acoustic spectrum which closes at an inflection point (line) that acts as an interior edge allowing a localized mode to emerge within the band gap. Unlike mechanisms of weak localization (44, 45) or well-known whispering gallery modes (30, 46) that rely sensitively on details of the domain geometry, our topological argument explains the existence of localized sound modes and their robustness against perturbations in the musical saw, providing a framework to explore not just topological mechanics but also dynamics in thin plates and shells.

The ability to control spatial geometry to trap modes at interfaces in the interior of the system offers a unique opportunity to design high-quality oscillators. As our results are material independent, they apply equally well to nanoscale electromechanical resonators (47, 48) and provide a geometric approach to design high-quality resonators without relying on intrinsic nonlinearities (49). Just as in the musical saw, in nanomechanical devices, dissipation can be dominated by radiation through the clamped boundary (43). Current on-chip topological nanoelectromechanical metamaterials use carefully patterned periodic arrays of nanomembranes to control localized modes in robust acoustic waveguides (50, 51). Our work suggests an alternate strategy inspired by the singing saw, which relies solely on the scale separation intrinsic to any curved thin sheet; by manipulating curvature spatially, topological modes localized in the interior hence remain vibrationally isolated and decay extremely slowly, allowing ultrahigh-quality oscillations, perhaps even in the ultimate limit of atomically thin graphene (52).

Materials and Methods

Extended data on the experiments and the details of the numerical modeling and theoretical calculations are provided in *SI Appendix*.

Saw Experiments. The wooden handle of the musical saw (Wentworth) was clamped onto an optical table, while the tapered end of the blade was attached to a sliding metal bracket mounted onto a vertical guide rail. Cork discs (around 2 cm in diameter and 0.5 to 1 cm in thickness) were used to cushion and softly support the clamped end of the blade. This helped damp out oscillations at the saw end and reduced any high-frequency ringing arising from direct metal-on-metal contact. The saw blade was bent into two configurations, a J shape (Fig. 1*B*) and an S shape (Fig. 1*C*), and manually either struck with a mallet or bowed with a violin bow at the straight edge, both near the center of the blade. The blade was allowed to freely ringdown postexcitation. The audio was recorded using a USB microphone (Fifine technology, K669-K669B, sampling frequency $f_s = 44.1$ kHz) placed near the saw and analyzed using the software Audacity.

Multiple measurements of the ringdown signal, each lasting 5 to 6 s, were made with a gap of a few seconds between runs. A separate 10 to 15 s audio sample with a stationary saw was used as a template to filter any background noise using the in-built noise reduction functionality in Audacity. The denoised audio samples were then analyzed using a custom Python code. Both left and right (stereo) channels are strongly correlated with each other, so we simply averaged the two to get the signal for each run. Upon using a Hann window and Fourier transforming each signal, we binned the frequency axis with a bin size of $\Delta\omega = 5$ Hz and averaged the normalized (by the maximum) magnitude of the Fourier transform over different runs ($N = 26$: J shape, mallet; $N = 28$: S shape, bow).

The average spectrum (normalized) is plotted in Fig. 3 *C* and *D*, *Top*, with the shaded region corresponding to the SE over the independent runs. The spectrograms in Fig. 1 *D*, *Middle* and *Right*, were computed for individual audio signals using matplotlib's specgram function with options NFFT = 512 Hz (number of fast Fourier transform data points per block), pad_to = 8, 192 Hz, and noverlap = 256 Hz. In order to compute the decay time of the sound, we normalized each time series by its maximum (in magnitude) and lined them up so $t = 0$ is at the maximum of the signal. We averaged the absolute value of the temporally aligned signals over independent runs and performed an additional moving average over a time step $\Delta t = 0.025$ s to smooth out all the high-frequency oscillations, leaving behind only the required envelope. This smoothed average curve (once again normalized by its maximum) is shown in dark blue in Fig. 3 *C* and *D*, *Bottom*. A similar calculation and smoothing is also done for the SE computed over independent runs and is plotted as the shaded region about the average. The smoothed average time series is then fit to an exponential function with a constant offset using SciPy's in-built nonlinear curve fitting function. The errors on our estimate for the dominant frequency (ω_0) and the decay time (τ) arise primarily from the chosen resolution of our smoothing windows ($\Delta\omega$, Δt) as other sources of measurement error are much smaller. We have nonetheless checked that our choice of the window size ($\Delta\omega$, Δt) is optimum as changing it by small amounts does not affect our results, but decreasing Δt by an order of magnitude significantly degrades the exponential fit.

Data Availability. Code and data reproducing the results in this paper have been deposited on Figshare, https://doi.org/10.6084/m9.figshare.19441385, and are described in the article and supporting information.

ACKNOWLEDGMENTS. S.S. is supported by the Harvard Society of Fellows. S.S. thanks Vincenzo Vitelli for helpful discussions and gratefully acknowledges useful interactions during the virtual 2021 Kavli Institute of Theoretical Physics program "The Physics of Elastic Films: From Biological Membranes to Extreme Mechanics," supported in part by the NSF under Grant NSF PHY-1748958. L.M. acknowledges Grants NSF DMR 2011754 and NSF DMR 1922321, the Simons Foundation, and the Henri Seydoux Fund for partial financial support.

Author affiliations: [a]Department of Physics, Harvard University, Cambridge, MA 02138; [b]Paulson School of Engineering and Applied Sciences, Harvard University, Cambridge, MA 02138; and [c]Department of Organismic and Evolutionary Biology, Harvard University, Cambridge, MA 02138

1. N. H. Fletcher, T. Rossing, *The Physics of Musical Instruments* (Springer New York, 2008).
2. G. Johnson, *Saw, Musical* (Grove Music Online, Oxford University Press, 2001).
3. J. J. Leonard, J. Graebner, *Scratch My Back: A Pictoral History of the Musical Saw and How to Play It.* (Kaleidoscope Press), ed. 1 (1989).
4. R. Cook, Vibration of a segment of a non-circular cylindrical shell: The "musical saw" problem. *J. Sound Vibrat.* **146**, 339–341 (1991).
5. A. Tubis, R. E. Davis, The musical saw-operational features and simple dynamical theory. *J. Acoust. Soc. Am.* **71**, S82–S83 (1982).
6. J. F. M. Scott, J. Woodhouse, Vibration of an elastic strip with varying curvature. *Phil. Trans. R. Soc. A* **339**, 587–625 (1992).
7. W. T. Koiter, "A consistent first approximation in the general theory of thin elastic shells" in *Proceedings of I.U.T.A.M. Symposium on the Theory of Thin Elastic Shells*, W. T. Koiter, Ed. (North-Holland, Amsterdam, 1960), pp. 12–33.

8. B. Audoly, Y. Pomeau, *Elasticity and Geometry: From Hair Curls to the Non-linear Response of Shells* (Oxford University Press, 2010).
9. R. Worland, The musical saw and the flexatone: An experimental study of confined vibrational modes in metal plates of variable curvature. *J. Acoust. Soc. Am.* **139**, 2011–2011 (2016).
10. R. Worland, The musical saw: Musical acoustics of trapped vibrational modes in a curved blade. *J. Acoust. Soc. Am.* **145**, 1750–1750 (2019).
11. D. J. Thouless, M. Kohmoto, M. P. Nightingale, M. den Nijs, Quantized hall conductance in a two-dimensional periodic potential. *Phys. Rev. Lett.* **49**, 405 (1982).
12. M. Z. Hasan, C. L. Kane, Colloquium: Topological insulators. *Rev. Mod. Phys.* **82**, 3045 (2010).
13. X. L. Qi, S. C. Zhang, Topological insulators and superconductors. *Rev. Mod. Phys.* **83**, 1057 (2011).
14. C. Kane, T. Lubensky, Topological boundary modes in isostatic lattices. *Nat. Phys.* **10**, 39–45 (2014).
15. S. D. Huber, Topological mechanics. *Nat. Phys.* **12**, 621–623 (2016).
16. X. Mao, T. C. Lubensky, Maxwell lattices and topological mechanics. *Annu. Rev. Condens. Matter Phys.* **9**, 413–433 (2018).
17. G. Ma, M. Xiao, C. T. Chan, Topological phases in acoustic and mechanical systems. *Nat. Rev. Phys* **1**, 281–294 (2019).
18. D. Bartolo, D. Carpentier, Topological elasticity of nonorientable ribbons. *Phys. Rev. X* **9**, 041058 (2019).
19. A. Saremi, Z. Rocklin, Topological elasticity of flexible structures. *Phys. Rev. X* **10**, 011052 (2020).
20. K. Sun, X. Mao, Continuum theory for topological edge soft modes. *Phys. Rev. Lett.* **124**, 207601 (2020).
21. K. Sun, X. Mao, Fractional excitations in non-Euclidean elastic plates. *Phys. Rev. Lett.* **127**, 098001 (2021).
22. P. Delplace, J. B. Marston, A. Venaille, Topological origin of equatorial waves. *Science* **358**, 1075–1077 (2017).
23. S. Shankar, M. J. Bowick, M. C. Marchetti, Topological sound and flocking on curved surfaces. *Phys. Rev. X* **7**, 031039 (2017).
24. A. Souslov, K. Dasbiswas, M. Fruchart, S. Vaikuntanathan, V. Vitelli, Topological waves in fluids with odd viscosity. *Phys. Rev. Lett.* **122**, 128001 (2019).
25. S. Shankar, A. Souslov, M. J. Bowick, M. C. Marchetti, V. Vitelli, Topological active matter. arXiv [Preprint] (2020). https://arxiv.org/abs/2010.00364 (Accessed 7 April 2022).
26. R. Süsstrunk, S. D. Huber, Observation of phononic helical edge states in a mechanical topological insulator. *Science* **349**, 47–50 (2015).
27. M. Miniaci, R. Pal, B. Morvan, M. Ruzzene, Experimental observation of topologically protected helical edge modes in patterned elastic plates. *Phys. Rev. X* **8**, 031074 (2018).
28. R. K. Pal, M. Ruzzene, Edge waves in plates with resonators: An elastic analogue of the quantum valley hall effect. *New J. Phys.* **19**, 025001 (2017).
29. H. Nassar *et al.*, Nonreciprocity in acoustic and elastic materials. *Nat. Rev. Mater.* **5**, 667–685 (2020).
30. J. W. S. B. Rayleigh, *The Theory of Sound* (Macmillan, 1896), vol. 2.
31. A. A. Evans, A. J. Levine, Reflection and refraction of flexural waves at geometric boundaries. *Phys. Rev. Lett.* **111**, 038101 (2013).
32. P. G. Ciarlet, *Theory of Shells, Mathematical Elasticity.* (Elsevier Science, 2000).
33. J. Kernes, A. J. Levine, Effects of curvature on the propagation of undulatory waves in lower dimensional elastic materials. *Phys. Rev. E* **103**, 013002 (2021).
34. R. Süsstrunk, S. D. Huber, Classification of topological phonons in linear mechanical metamaterials. *Proc. Natl. Acad. Sci. U.S.A.* **113**, E4767–E4775 (2016).
35. T. Frankel, *The Geometry of Physics: An introduction* (Cambridge University Press, 2011).
36. M. Nakahara, *Geometry, Topology and Physics* (CRC Press, 2018).
37. L. Fu, C. L. Kane, Topological insulators with inversion symmetry. *Phys. Rev. B Condens. Matter Mater. Phys.* **76**, 045302 (2007).
38. L. Fu, Topological crystalline insulators. *Phys. Rev. Lett.* **106**, 106802 (2011).
39. T. L. Hughes, E. Prodan, B. A. Bernevig, Inversion-symmetric topological insulators. *Phys. Rev. B Condens. Matter Mater. Phys.* **83**, 245132 (2011).
40. P. M. Naghdi, "Foundations of elastic shell theory" in *Progress in Solid Mechanics*, I. N. Sneddon, R. Hill, Eds. (North-Holland, Amsterdam, 1963), vol. 4, pp. 1–90.
41. M. S. Alnæs *et al.*, The FEniCS project version 1.5. *Arch. Numer. Softw.* **3**, 9–23 (2015).
42. J. S. Hale, M. Brunetti, S. P. A. Bordas, C. Maurini, Simple and extensible plate and shell finite element models through automatic code generation tools. *Comput. Struc.* **209**, 163–181 (2018).
43. I. Wilson-Rae *et al.*, High-Q nanomechanics via destructive interference of elastic waves. *Phys. Rev. Lett.* **106**, 047205 (2011).
44. S. M. Heilman, R. S. Strichartz, Localized eigenfunctions: Here you see them, there you don't. *Not. Am. Math. Soc.* **57**, 624–629 (2010).
45. M. Filoche, S. Mayboroda, Universal mechanism for Anderson and weak localization. *Proc. Natl. Acad. Sci. U.S.A.* **109**, 14761–14766 (2012).
46. L. Rayleigh, Cxii. The problem of the whispering gallery. *Lond. Edinb. Dublin Philos. Mag. J. Sci.* **20**, 1001–1004 (1910).
47. H. G. Craighead, Nanoelectromechanical systems. *Science* **290**, 1532–1536 (2000).
48. K. L. Ekinci, Electromechanical transducers at the nanoscale: Actuation and sensing of motion in nanoelectromechanical systems (NEMS). *Small* **1**, 786–797 (2005).
49. R Lifshitz, M. C. Cross, "Nonlinear dynamics of nanomechanical and micromechanical resonators" in *Review of Nonlinear Dynamics Complexity*, H. G. Schuster, Ed. (Wiley, 2008), pp. 1–48.
50. J. Cha, K. W. Kim, C. Daraio, Experimental realization of on-chip topological nanoelectromechanical metamaterials. *Nature* **564**, 229–233 (2018).
51. J. Ma, X. Xi, Y. Li, X. Sun, Nanomechanical topological insulators with an auxiliary orbital degree of freedom. *Nat. Nanotechnol.* **16**, 576–583 (2021).
52. J. S. Bunch *et al.*, Electromechanical resonators from graphene sheets. *Science* **315**, 490–493 (2007).

PNAS
www.pnas.org

Supplementary Information for

Geometric control of topological dynamics in a singing saw

Suraj Shankar, Petur Bryde, and L. Mahadevan

Correspondence and requests for materials should be addressed to L. Mahadevan.
E-mail: lmahadev@g.harvard.edu

This PDF file includes:

Supplementary text
Figs. S1 to S5
SI References

Supporting Information Text

1. Saw experiments

In addition to the measurements presented in the main text (mallet on the J-shape, bow on the S-shape), we have the two other possible combinations as well: J-shape with a bow and an S-shape with a mallet. A plot of the normalized audio signal time series is shown in Fig. S1A for a representative run of all four cases (the green and black curves are the same as in the Fig. 1D). The J-shape cannot be reliably bowed to produce sound in a reproducible fashion, and requires excessive force when bowing to elicit any sound, if at all. As can be seen from Figs. S1A-B, the sound is extremely short lived (it dies within ~ 20 ms once the bow stops, which is of the order of our smoothing window Δt) and is also very high pitched (~ 3 kHz, Fig. S1B). We expect that the bow excites very high frequency bulk delocalized modes above the band gap, which dissipate away very rapidly. As this mode of excitation is not consistently reproducible, we do not analyze it further.

The S-shape can be excited with a mallet as well, though its acoustic quality isn't as clear as when the saw is bowed. Here we obtained $N = 9$ independent runs for a different saw setup in an S-shape (Fig. S1C, top left), similar to the one in Fig. 1C. When struck with a mallet, however lightly, the saw rings with the distinctive sustained note, but in addition, one also hears clear vibrato or beats due to the blade flexing and the inflection point itself moving. This leads to closely spaced peaks in the Fourier spectrum (Fig. S1C, right), with the primary frequency $\omega_0 = 580 \pm 2.5$ Hz and the secondary frequency $\omega_1 = 590 \pm 2.5$ Hz. The same beats can be seen in the smoothed decay of the signal amplitude (Fig. S1C, bottom left), where the zoomed-in inset shows small scale low frequency oscillations with a period ~ 0.1 s (or equivalently, ~ 10 Hz). This vibrato-like effect is not present when the clamped S-shape saw is bowed, but occurs almost inevitably when the saw is manually struck with a mallet, and it presumably causes higher dissipation in the interior of the saw as well. As a result, while we can compute the Q-factor with this mode of excitation ($\mathrm{Q} = 79.3 \pm 7.6$, Fig. S1), it is smaller than the value obtained when the saw is bowed ($\mathrm{Q} = 153.5 \pm 8.1$, Fig. 3D), but it still exceeds the J-shape saw struck by a mallet ($\mathrm{Q} = 10.6 \pm 1.4$, Fig. 3C), by a factor of ~ 8. Hence, while the details of the excitation mechanism and potential nonlinear effects do quantitatively affect the Q-factor, the qualitative feature remains that the S-shape saw with an inflection point behaves as a more robust and high quality resonator than a blade with single sign curvature (J-shape).

2. Computational Naghdi shell model

Here we provide a brief derivation and description of the full geometrically nonlinear Naghdi model that we use for our numerical computations. The computations are carried out using a finite element method, with a custom code employing the FEniCS (S1, S2) and FEniCS-shells (S3) libraries. The numerical implementation details are described later in Sec. D.

A. Differential geometry of a deforming shell. We adopt the convention that Latin indices denote components of surface tensors and take values in $\{1, 2\}$, while Greek indices denote components of 3D tensors and take values in $\{1, 2, 3\}$. Repeated indices are summed as usual. The shell is defined as a three-dimensional (3D) slender elastic body specified by a reference surface $\mathcal{S}$, representing the midsurface of the undeformed shell, and a constant thickness h, which is assumed small compared to the lateral dimensions and radius of curvature of the shell. The midsurface is parametrized by its embedding in Euclidean space, given by a map $\mathbf{X}_0 : \Omega_0 \to \mathbb{R}^3$ where the *reference domain* Ω_0 is a bounded domain in $\mathbb{R}^2$. At any point on the midsurface, the vectors $\mathbf{e}_i = \partial_i \mathbf{X}_0$ are linearly independent, and thus form a basis for the tangent plane, which is the covariant basis for the midsurface. The unit normal field to the reference surface is simply $\hat{\mathbf{n}} = (\mathbf{e}_1 \times \mathbf{e}_2)/|\mathbf{e}_1 \times \mathbf{e}_2|$. A material point within the undeformed shell is then parametrized by

$$\mathbf{R}_0(\xi^1, \xi^2, \xi^3) = \mathbf{X}_0(\xi^1, \xi^2) + \xi^3 \hat{\mathbf{n}}(\xi^1, \xi^2) \ , \quad (\xi^1, \xi^2, \xi^3) \in \Omega := \Omega_0 \times \left[-\frac{h}{2}, \frac{h}{2}\right] \ , \tag{S1}$$

where ξ^α are the local 3D coordinates within the material. The first and second fundamental forms of the reference midsurface are

$$a_{ij} = \partial_i \mathbf{X}_0 \cdot \partial_j \mathbf{X}_0 \ , \quad b_{ij} = \hat{\mathbf{n}} \cdot \partial_i \partial_j \mathbf{X}_0 \ . \tag{S2}$$

The reference area element of the surface is $\mathrm{d}A = \sqrt{\det(\mathbf{a})}\mathrm{d}\xi^1 \mathrm{d}\xi^2$. All the index raising and lowering in the midsurface is performed using a_{ij}. The 3D reference metric tensor $g_{\alpha\beta} = \partial_\alpha \mathbf{R}_0 \cdot \partial_\beta \mathbf{R}_0$ has a simple expansion in ξ^3,

$$g_{ij} = a_{ij} - 2\xi^3 b_{ij} + (\xi^3)^2 b_i^k b_{kj} \ , \quad g_{i3} = 0 \ , \quad g_{33} = 1 \ . \tag{S3}$$

B. Kinematics. We let $U_\alpha(\boldsymbol{\xi})$ be the 3D displacement of the material points within the shell (the deformed position is then $\mathbf{R} = \mathbf{R}_0 + \mathbf{U}$). To reduce the dimensionality of the model, we employ the Reissner–Mindlin kinematic assumption (S4–S6), which specifies the displacement $\mathbf{U}$ of an arbitrary point of the shell in terms of a tangential displacement vector field u_i, a normal deflection of the midsurface f and a rotation of the unit normal θ_i, all defined on the midsurface. Specifically, we assume that the displacement takes the form

$$\mathbf{U} = (u^i + \xi^3 \theta^i)\mathbf{e}_i + f\hat{\mathbf{n}} \ . \tag{S4}$$

In words, the assumption states that a material line initially normal to the midsurface remains straight and unstretched in the deformed state, but may be translated and rotated. We see that (u_i, f) prescribes the translation of the midsurface while θ_i are the rotations of the material line around the axes defined by the reference tangent vectors $\mathbf{e}_i$ (see Fig. S4). The full

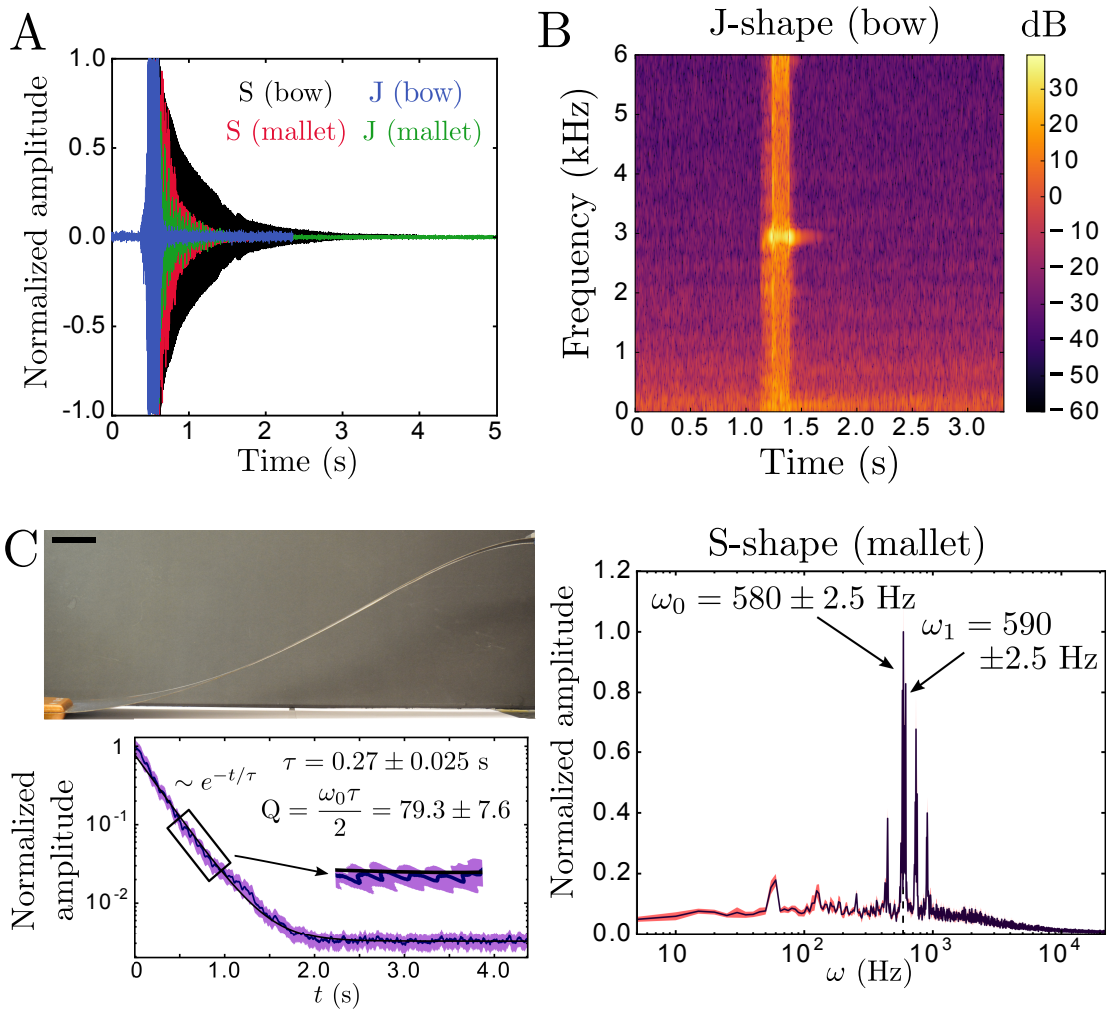

Fig. S1. (A) Normalized audio signal time series (all aligned in time so their maxima prior to the decay coincide) for different excitation modes on different saw configurations: S-shape with the bow (black), S-shape with a mallet (red), J-shape with a bow (blue) and J-shape with a mallet (green). (B) Spectrogram corresponding to a bowed J-shape saw, which can produce a shortly lived, high frequency (~ 3 kHz) sound. (C) The saw clamped in an S-shape used for the audio recordings involving the mallet (top left, scale bar: 5 cm). The normalized average of the ringdown signal (shaded region is the standard error, $N = 9$), along with an exponential fit to extract the decay time $\tau = 0.27 \pm 0.025$ s (bottom left). Inset shows a zoomed-in part of the curve displaying periodic low frequency oscillations (~ 10 Hz) associated with the beats or vibrato effect obtained upon striking the saw with a mallet. The corresponding average Fourier spectrum (averaged, shaded region is standard error) showing closely spaced sharp peaks at $\omega_0 = 580 \pm 2.5$ Hz (most dominant) and $\omega_1 = 590 \pm 2.5$ Hz (second), with the frequency separation signalling the persistent beats or vibrato like phenomena present in these measurements. The measured Q-factor ($Q = 79.3 \pm 7.6$) is smaller than the case of a similar S-shape saw excited with the violin bow ($Q = 153.5 \pm 8.1$, Fig. 3D), but is still larger than the J-shape saw excited by a mallet ($Q = 10.6 \pm 1.4$, Fig. 3C).

nonlinear strain tensor is defined by $E_{\alpha\beta} = (1/2)(\bar{g}_{\alpha\beta} - g_{\alpha\beta})$, where $\bar{g}_{\alpha\beta} = \partial_\alpha \mathbf{R} \cdot \partial_\beta \mathbf{R}$ is the actual metric of the deformed configuration. To leading order in variations along the thickness (i.e., ξ^3), we obtain

$$\begin{aligned} E_{ij} &= \varepsilon_{ij} + \xi^3 C_{ij} + \mathcal{O}\left((\xi^3)^2\right) \ , \\ E_{i3} &= S_i \ , \\ E_{33} &= 0 \ , \end{aligned} \qquad [S5]$$

where ε_{ij} is the in-plane strain, C_{ij} is the curvature or bending strain and S_i is the transverse shear strain. The linearized (in displacement) forms of these strains is given by

$$\varepsilon_{ij} = \frac{1}{2}\left(\nabla_i u_j + \nabla_j u_i\right) - b_{ij} f \ , \qquad [S6a]$$

$$C_{ij} = \frac{1}{2}\left(\nabla_i \theta_j + \nabla_j \theta_i - b_i^k \nabla_j u_k - b_j^k \nabla_i u_k\right) + b_i^k b_{kj} f \ , \qquad [S6b]$$

$$S_i = \frac{1}{2}\left(\theta_i + \nabla_i f + b_i^k u_k\right) \ , \qquad [S6c]$$

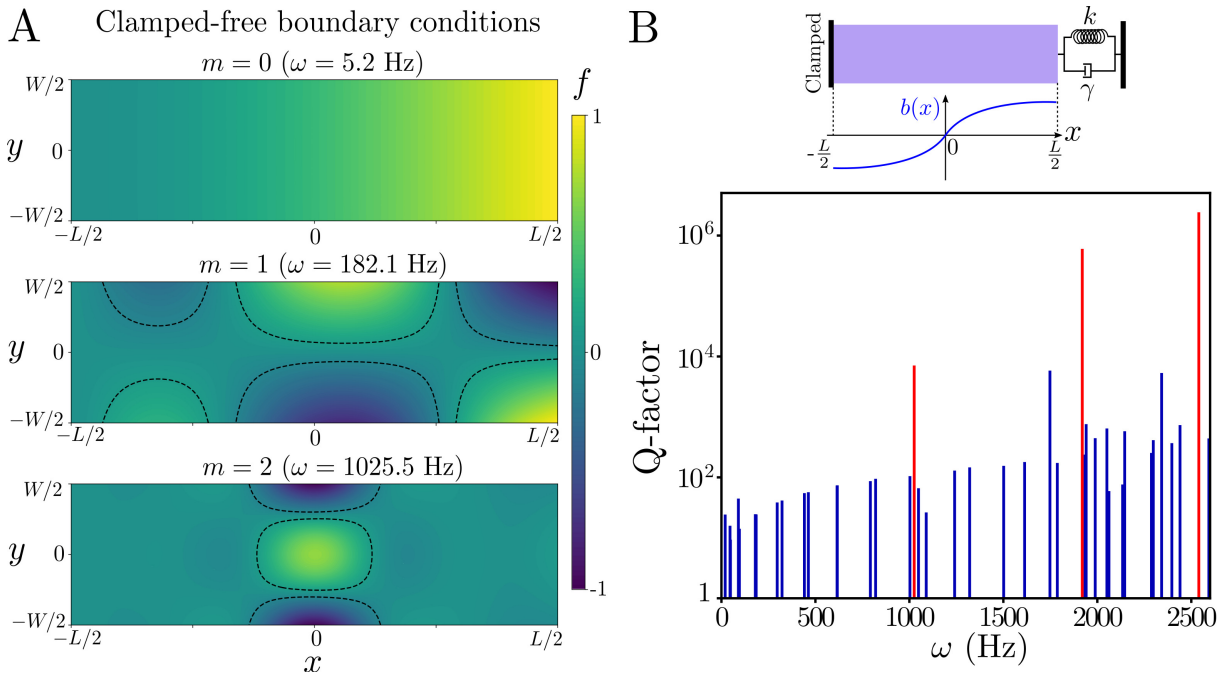

Fig. S2. (A) Numerically computed acoustic eigenmodes for a saw with a curvature profile $b(x) = b_0 \tanh(x/\ell)$ ($b_0 L = 0.5$, $\ell/L = 0.1$, $L = 1$ m) and asymmetric boundary conditions, i.e., the left end is clamped, but the right end is free. The $m = 0, 1$ modes (top and middle), as before, are linearized isometries and they delocalize over the entire saw. As a result, they are strongly affected by the boundary conditions. On the other hand, the first localized mode with $m = 2$ is trapped at the inflection point, and is hence virtually unaffected by the boundary conditions (bottom, see also Fig. 2C). The dashed black lines are 10% isocontours of f. (B) The free end of the saw (with the same curvature profile) is modified to now include a soft restoring spring (k) and a frictional dashpot (γ) for both the in-plane stress and the bending moment (top). Once again, we see a dramatic enhancement of the Q-factor (bottom) by a few orders of magnitude when the localized modes are excited (red), compared to when the delocalized bulk modes are excited (blue).

as also depicted in Fig. 1E. The covariant derivatives are compatible with the reference metric a_{ij} of the shell. They are defined in terms of the Christoffel symbols $\Gamma^k_{ij} = \partial_j \mathbf{e}_i \cdot \mathbf{e}^k$ in the usual way:

$$\nabla_i u_j = \partial_i u_j - \Gamma^k_{ij} u_k \qquad \text{[S7]}$$

Remarks. (i) In the case of a flat plate, the second fundamental form b_{ij} vanishes and Eqs. S5-S6 reduce to the usual strain tensor of the Reissner–Mindlin plate model (S4, S5). Note that in this case, the in-plane membrane strain tensor ε_{ij} depends only on the in-plane displacement u_i and is uncoupled from the bending and shearing strains. (ii) A displacement field of the form given in Eq. S4 where $\theta_i = -\nabla_i f - b^k_i u_k$ is said to satisfy the Kirchhoff–Love kinematic assumption (S8, S9). It is stronger than the Reissner–Mindlin hypothesis as it imposes that a material line which is initially normal to the midsurface remains normal in the deformed state as well. From Eq. S6c, this is equivalent to the transverse shear strain S_i vanishing. (iii) If the displacement field satisfies the Kirchhoff–Love assumption and the shell is flat ($a_{ij} = \delta_{ij}$, $b_{ij} = 0$), we obtain the Kirchhoff–Love plate model (S10, S11).

C. Governing equations. We derive the dynamical Naghdi equations starting from the continuum mechanics of the three-dimensional shell body. The constitutive relation for the 3D stress tensor $\Sigma^{\alpha\beta} = H^{\alpha\beta\mu\nu} E_{\mu\nu}$ involves the elastic tensor (for an isotropic material)

$$H^{\alpha\beta\mu\nu} = \frac{Y}{2(1+\nu)} \left[g^{\alpha\mu} g^{\beta\nu} + g^{\alpha\nu} g^{\beta\mu} + \frac{2\nu}{(1-2\nu)} g^{\alpha\beta} g^{\mu\nu} \right] , \qquad \text{[S8]}$$

where Y and ν are the Young's modulus and Poisson's ratio of the material, respectively. Upon using the expression for the 3D metric tensor (Eq. S3) in Eq. S8, along with the standard additional assumption that the normal stress Σ^{33} vanishes everywhere, we get

$$\Sigma^{ij} = \tilde{A}^{ijk\ell} E_{k\ell} , \quad \Sigma^{i3} = \frac{1}{2} \tilde{B}^{ij} E_{j3} , \qquad \text{[S9]}$$

with the reduced elastic tensors

$$\tilde{A}^{ijk\ell} = \frac{Y}{2(1+\nu)} \left(g^{ik} g^{j\ell} + g^{i\ell} g^{kj} + \frac{2\nu}{(1-\nu)} g^{ij} g^{k\ell} \right) , \quad \tilde{B}^{ij} = \frac{2Y}{1+\nu} g^{ij} . \qquad \text{[S10]}$$

Newton's second law for the 3D shell reads

$$\rho \partial_t^2 \mathbf{U} = \boldsymbol{\nabla} \cdot \boldsymbol{\Sigma} + \mathbf{F} , \qquad \text{[S11]}$$

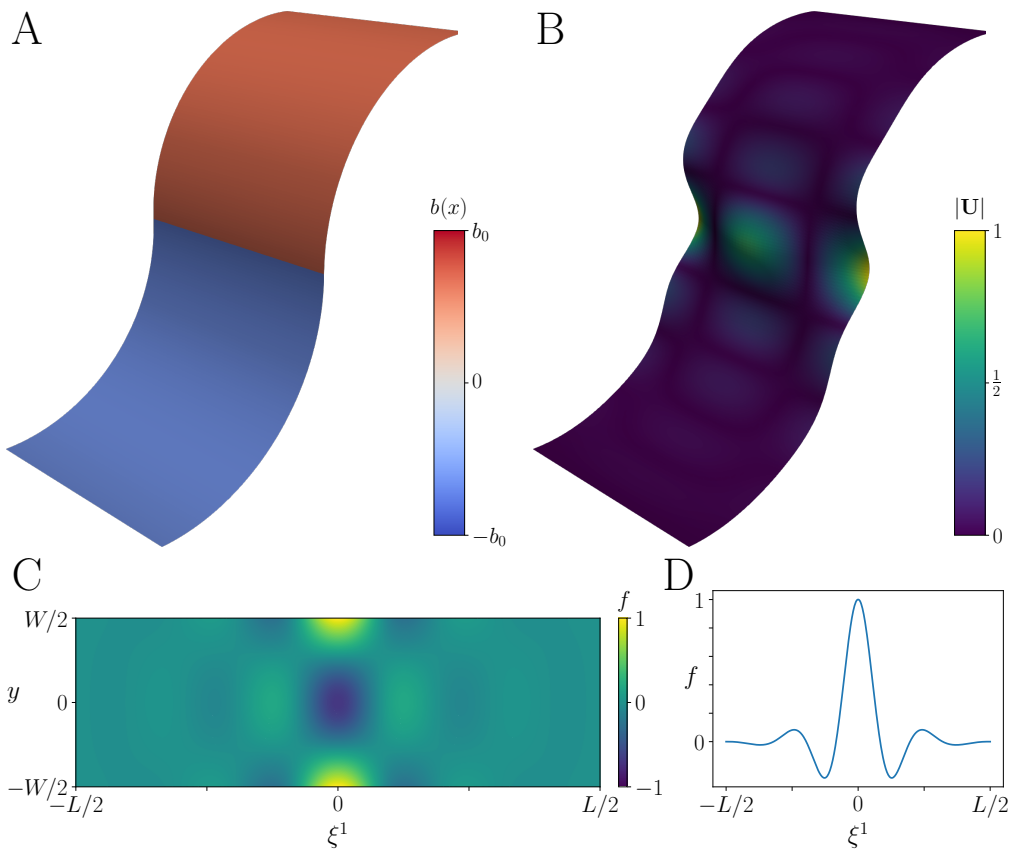

Fig. S3. (A) A saw with a discontinuous curvature profile $b(x) = b_0\,\mathrm{sgn}(x)$, corresponding to the "sharp domain wall" limit $\ell \to 0$ ($b_0 = 5$ m^{-1}, $L = 0.63$ m). (B) Numerically computed eigenmode ($\omega = 3729$ Hz, color is the normalized 3D displacement) of the saw for clamped-clamped boundary conditions showing strong confinement near the domain wall. (C) The normal component f (normalized) of the same mode as a function of the two curvilinear coordinates ξ^1 and $\xi^2 = y$. Here ξ^1 is measured along the long direction, but cannot be identified with the x-coordinate due to the large curvature. (D) Plot of the normal deflection of the saw at $y = W/2$ along ξ^1.

where ρ is the mass density and $\mathbf{F}$ is an external force density on the shell. To obtain a weak form of the equation, suitable for the finite element method, we introduce a test vector field $\mathbf{V}$ satisfying the same kinematic assumptions as $\mathbf{U}$, i.e., $\mathbf{V} = (v^i + \xi^3\eta^i)\mathbf{e}_i + v_n\hat{\mathbf{n}}$, as well as the same essential boundary conditions, described below. Upon taking the inner product of Eq. S11 with $\mathbf{V}$ and integrating by parts, we obtain

$$\int_\Omega \mathrm{d}V \rho\partial_t^2\mathbf{U}\cdot\mathbf{V} + \int_\Omega \mathrm{d}V\ \boldsymbol{\Sigma}(\mathbf{U}) : \mathbf{E}(\mathbf{V}) = \int_\Omega \mathrm{d}V\ \mathbf{F}\cdot\mathbf{V} + \int_{\partial\Omega} \mathrm{d}S\ \left(\boldsymbol{\Sigma}(\mathbf{U})\cdot\hat{\boldsymbol{\nu}}\right)\cdot\mathbf{V}\ . \tag{S12}$$

where $\mathrm{d}V = \sqrt{\det(\mathbf{g})}\mathrm{d}\xi^1\mathrm{d}\xi^2\mathrm{d}\xi^3$ is the volume element and $\hat{\boldsymbol{\nu}}$ is the unit outward normal along the boundary of the 3D shell, with $\mathrm{d}S$ the boundary area element. We will temporarily assume vanishing tractions $\boldsymbol{\Sigma}(\mathbf{U})\cdot\hat{\boldsymbol{\nu}}$, so that the last term vanishes. This term will be reintroduced below where we discuss the dissipative spring boundary conditions.

Upon expanding the second term on the left-hand side of Eq. S12, and integrating over the thickness of the shell (to leading order in ξ^3, conversely h), we obtain the dynamic Naghdi equations in weak form

$$\begin{aligned}\int_{\Omega_0} \mathrm{d}A\ \rho h\left(\partial_t^2 u_i v^i + \partial_t^2 f v_n\right) + \int_{\Omega_0} \mathrm{d}A\ h\mathcal{A}^{ijk\ell}\left[\varepsilon_{ij}(\mathbf{u},f)\varepsilon_{k\ell}(\mathbf{v},v_n) + \frac{h^2}{12}C_{ij}(\mathbf{u},f,\boldsymbol{\theta})C_{k\ell}(\mathbf{v},v_n,\boldsymbol{\eta})\right]\\ + \int_{\Omega_0} \mathrm{d}A\ h\mathcal{B}^{ij}S_i(\mathbf{u},f,\boldsymbol{\theta})S_j(\mathbf{v},v_n,\boldsymbol{\eta}) = \int_{\Omega_0} \mathrm{d}A\ h(F_i v^i + F_n v_n)\ ,\end{aligned} \tag{S13}$$

where $\mathbf{F} = F^i\mathbf{e}_i + F_n\hat{\mathbf{n}}$, $\mathrm{d}A = \sqrt{\det(\mathbf{a})}\mathrm{d}\xi^1\mathrm{d}\xi^2$ is the area element on the midsurface and $\mathcal{A}, \mathcal{B}$ are the restrictions of the elastic tensors $\tilde{A}, \tilde{B}$ onto the midsurface, i.e.,

$$\mathcal{A}^{ijk\ell} = \frac{Y}{2(1+\nu)}\left(a^{ik}a^{j\ell} + a^{i\ell}a^{jk} + \frac{2\nu}{(1-\nu)}a^{ij}a^{k\ell}\right)\ ,\quad \mathcal{B}^{ij} = \frac{2Y}{(1+\nu)}a^{ij}\ . \tag{S14}$$

The Naghdi equations can also be written as a boundary value problem in strong form, as shown in (S12).

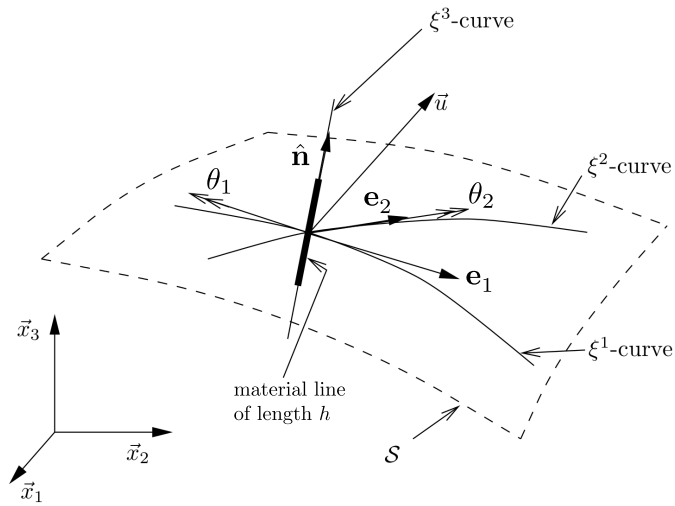

Fig. S4. The kinematic assumptions for the Naghdi shell model (adapted from Ref. (S7)).

For convenience, we will use the shorthand $u = (\mathbf{u}, f, \boldsymbol{\theta})$, $v = (\mathbf{v}, v_n, \boldsymbol{\eta})$, and let k_m, k_b and k_s denote the membrane, bending and shear terms of Eq. S13:

$$\begin{aligned} k_m(u,v) &= \int_{\Omega_0} \mathrm{d}A\; h\mathcal{A}^{ijk\ell}\varepsilon_{ij}(\mathbf{u}, f)\varepsilon_{k\ell}(\mathbf{v}, v_n) \\ k_b(u,v) &= \int_{\Omega_0} \mathrm{d}A\; \mathcal{A}^{ijk\ell}\frac{h^3}{12}C_{ij}(\mathbf{u}, f, \boldsymbol{\theta})C_{k\ell}(\mathbf{v}, v_n, \boldsymbol{\eta}) \\ k_s(u,v) &= \int_{\Omega_0} \mathrm{d}A\; h\mathcal{B}^{ij}S_i(\mathbf{u}, f, \boldsymbol{\theta})S_j(\mathbf{v}, v_n, \boldsymbol{\eta}). \end{aligned} \qquad \text{[S15]}$$

Remark. (i) Note that in Eq. S13, the bending term k_b is of higher order in the thickness h compared to the stretching and shearing terms, a general feature of shell models (S6, S11, S13). In the limit of small thickness, modes with vanishing membrane and shear strains are energetically favorable. In the linear theory, these pure-bending modes are characterized by $\boldsymbol{\varepsilon} = \mathbf{0}$, and $\boldsymbol{\theta} = -(\boldsymbol{\nabla} f + \mathbf{b}\cdot\mathbf{u})$. Existence of pure-bending displacements depends on the boundary conditions as well as the midsurface reference geometry, in particular the sign of the Gaussian curvature $K_G = \det(\mathbf{b})/\det(\mathbf{a})$ (S7). Note, unlike incompatible non-Euclidean sheets (S14, S15) which have multiple notions of potentially conflicting reference curvatures, here, both $\mathbf{a}$ and $\mathbf{b}$ are compatible fundamental forms due to the existence of a reference configuration (and not just a reference geometry). Isometric bending deformations are well understood for surfaces where K_G has a constant sign, but less is known for surfaces of mixed type where K_G changes sign. (ii) If we replace the Reissner–Mindlin kinematic assumptions with the stronger Kirchhoff–Love assumption, we obtain instead the weak form of Koiter's equations (S7). An independent derivation of Koiter's equations in strong form is given in Sec. III. (iii) In the absence of curvature, the variational problem (Eq. S13) splits into two decoupled equations (in the linearized setting): a membrane problem for the in-plane displacement $\mathbf{u}$ and the remaining variables $(f, \boldsymbol{\theta})$ satisfy the Reissner–Mindlin plate equations. For the Kirchhoff–Love kinematic assumption, the latter further simplifies to the simple bending equation $\rho h\partial_t^2 f = -\kappa\nabla^4 f$, where $\kappa = Yh^3/[12(1-\nu^2)]$ is the bending rigidity.

We now describe the various boundary conditions. In all cases, the upper and lower faces of the shell (corresponding to $\xi^3 = \pm h/2$) are free, meaning that the traction $\boldsymbol{\Sigma}(\mathbf{U})\cdot\hat{\boldsymbol{\nu}}$ vanishes. We divide $\partial\Omega_0$ into three disjoint parts, $\partial\Omega_0 = \Gamma_0^c \cup \Gamma_0^f \cup \Gamma_0^d$ and let Γ^c, Γ^f, Γ^d be the corresponding portions of the lateral face, so that e.g. $\Gamma_c = \mathbf{R}_0(\Gamma_0^c \times [-h/2, h/2])$. The shell is subjected to clamped (Dirichlet) boundary conditions on Γ_c, meaning that the fields $(\mathbf{u}, f, \boldsymbol{\theta})$ vanish on Γ_0^c. In our numerical experiments, Γ_c is comprised of one or both short edges of the saw; we call the latter case clamped-clamped boundary conditions. The set Γ^f represents the free portion of the lateral face and always contains the long edges of the saw. It may also include one of the shorter edges in the case of clamped-free boundary conditions. In numerical experiments involving dissipation (see Fig. 3A-B and Fig. S2B), Γ^d coincides with the right edge of the saw where it is coupled to translational, rotational and torsional springs with distributed spring constants k, k_n and k_t and damping coefficients γ, γ_n and γ_t respectively. Specifically, the boundary term in Eq. S12 becomes

$$\int_{\partial\Omega} \mathrm{d}S\;\; (\boldsymbol{\Sigma}(\mathbf{U})\cdot\hat{\boldsymbol{\nu}})\cdot\mathbf{V} = -\int_{\Gamma_0^d} \mathrm{d}s\Big[h(kf + \gamma\partial_t f)v_n + \frac{(h)^3}{12}\big((k_n\theta_\perp + \gamma_\perp\partial_t\theta_\perp)\eta_\perp + (k_\parallel\theta_\parallel + \gamma_\parallel\partial_t\theta_\parallel)\eta_\parallel\big)\Big] \qquad \text{[S16]}$$

where $\theta_\perp$, $\theta_\parallel$ are the normal and tangential components of $\boldsymbol{\theta}$, and $\eta_\perp$, $\eta_\parallel$ are defined similarly.

Essential boundary conditions are imposed by specifying a solution space. Since the weak form of Naghdi's equations, Eq. S13, contains only first order derivatives, the appropriate space is $\mathcal{V} = \{(\mathbf{u}, f, \boldsymbol{\theta}) \in [H^1(\Omega_0)]^5 \colon u_i = f = \theta_i = 0 \text{ on } \Gamma_0^c\}$.

Defining the bilinear forms

$$
\begin{aligned}
m(u,v) &= \int_{\Omega_0} \mathrm{d}A\ \rho h \left(u_i v^i + f v_n\right), \\
k(u,v) &= k_m(u,v) + k_b(u,v) + k_s(u,v) - \int_{\Gamma_0^d} \mathrm{d}s \left[hkfv_n + \frac{(h)^3}{12}\left(k_\perp \theta_\perp \eta_\perp + k_\parallel \theta_\parallel \eta_\parallel\right)\right], \\
c(u,v) &= -\int_{\Gamma_0^d} \mathrm{d}s \left[h\gamma f v_n + \frac{(h)^3}{12}\left(\gamma_\perp \theta_\perp \eta_\perp + \gamma_\parallel \theta_\parallel \eta_\parallel\right)\right],
\end{aligned}
\tag{S17}
$$

and letting $F(v) = \int_{\Omega_0} \mathrm{d}A\ h(F_i v^i + F_n v_n)$, the Naghdi problem can be stated succinctly as: Find functions $u(x,t)$, twice differentiable in time, so that $u(\cdot,t) \in \mathcal{V}$ for all t and

$$
m(\partial_t^2 u, v) + c(\partial_t u, v) + k(u,v) = F(v) \tag{S18}
$$

for all $v \in \mathcal{V}$.

D. Numerical implementation. We discretize Eq. S18 in space using the finite element method. As previously mentioned, the weak form of the Naghdi equations admits solutions in H^1. However, it is well known that standard H^1-conforming finite element methods suffer from numerical locking when applied to shell models, which leads to overstiff behavior unless a very fine mesh is used. Several approaches to alleviate locking have been proposed, see (S3, S16, S17) and references therein. While no method has been rigorously shown to be locking free in all cases, numerical tests suggest that many of the known methods can successfully treat locking in the Naghdi model. Following (S3), we use a high-order partial selective reduced integration (PSRI) method, a variation of the technique introduced in (S16). This method was shown in (S16) to converge uniformly with respect to the shell thickness under some restrictive assumptions on the coefficients in the Naghdi model (see also (S18) for a related result). In the PSRI approach, second-order Lagrange finite elements augmented by cubic bubble functions are used for the displacements (u_1, u_2, f), and second-order Lagrange finite elements are used for the rotations (θ_1, θ_2). The stiffness form k in equation S18 is modified by splitting the membrane term k_m and shear term k_s into a weighted sum of two contributions, one of which is computed with a reduced integration. That is, we write k_m as

$$
\alpha \int_{\Omega_0} \mathrm{d}A\ h\mathcal{A}^{ijk\ell}\varepsilon_{ij}(\mathbf{u}, f)\varepsilon_{k\ell}(\mathbf{v}, v_n) + (1-\alpha)\int_{\Omega_0} \mathrm{d}A\ h\mathcal{A}^{ijk\ell}\varepsilon_{ij}(\mathbf{u}, f)\varepsilon_{k\ell}(\mathbf{v}, v_n)
$$

and compute the second integral using a reduced quadrature rule of order 2. The shear term k_s is similarly modified. The splitting parameter α is chosen as $h^2/\delta^2 \sim 0.05$ where δ is a typical element circumradius for the mesh, as suggested in (S3).

To solve the time-dependent problem, we integrate Eq. S18 in time using the Newmark-beta method (S19) with $\gamma = 1/2$, $\beta = 1/4$, which is second order accurate and unconditionally stable. Moreover, this scheme is symplectic, and known to have excellent energy behavior and long-time performance for systems that are conservative or weakly dissipative (S20). Therefore, it is particularly suitable for estimating the Q-factor of the lightly damped localized modes of the S-shaped saw. Combining this time-stepping scheme with the previously described spatial discretization yields a sequence of variational problems which are easily implemented in FEniCS. To compute the eigenmodes of the shell, we consider the eigenvalue problem obtained by taking the temporal Fourier transform of Eq. S18. This problem can be discretized in space in the same way as previously described, yielding a matrix eigenvalue problem which we solve using the SLEPc implementation of the Krylov-Schur algorithm (S21).

In our numerical simulations, we consider an elastic strip of length $L = 1$ m, width $W = 0.25$ m and thickness $h = 10^{-3}$ m. The material properties are $Y = 200$ GPa, $\nu = 0.3$ and $\rho = 7850$ kg/m^3, typical for mild steel. We use in each case a uniform triangular mesh, with the mesh size chosen so that the modes of interest have adequately converged; on the order of 15000 cells. In dynamic simulations, the time step was chosen $\Delta t \sim 50/f$ where f is the frequency of oscillation. In simulations where boundary damping was present, the spring coefficients k, $k_\perp$, $k_\parallel$ are chosen so that $khY^{-1} = 10^{-8}$, $k_\perp h^3 Y^{-1} = k_\parallel h^3 Y^{-1} = 10^{-11}$. The damping coefficients are chosen so that $\gamma/k = \gamma_\perp/k_\perp = \gamma_\parallel/k_\parallel = 10^{-2}$ s.

3. Topologically protected vibrations in thin shells

Here we describe the details of the analytical computations and topological characterization of the band structure of vibrating thin shells. In the limit of a very thin shell, we can neglect transverse shear deformations ($\mathbf{S} \approx \mathbf{0}$), and we work in the Kirchhoff–Love limit. The elastic energy then simply involves only stretching and bending terms (S11, S13, S22)

$$
E = \frac{Yh}{2(1-\nu^2)} \int \mathrm{d}A \left[\frac{1}{4}\|\mathbf{a}^{-1}\bar{\mathbf{a}} - \mathbf{1}\|_e^2 + \frac{h^2}{12}\|\mathbf{a}^{-1}(\bar{\mathbf{b}} - \mathbf{b})\|_e^2 \right], \tag{S19}
$$

where the matrix norm $\|\mathbf{A}\|_e^2 = \nu \mathrm{tr}^2(\mathbf{A}) + (1-\nu)\mathrm{tr}(\mathbf{A}^2)$ involves the Poisson ratio ν, for any matrix $\mathbf{A}$. As before, for a geometrically compatible shell, the reference metric ($a_{ij} = \partial_i \mathbf{X}_0 \cdot \partial_j \mathbf{X}_0$) and reference curvature tensor ($b_{ij} = \hat{\mathbf{n}} \cdot \partial_i \partial_j \mathbf{X}_0$), both derive from a rest configuration $\mathbf{X}_0$. The actual deformed configuration is instead characterized by the real metric $\bar{a}_{ij} = \partial_i \mathbf{X} \cdot \partial_j \mathbf{X}$ and the real curvature tensor $\bar{b}_{ij} = \hat{\mathbf{N}} \cdot \partial_i \partial_j \mathbf{X}$, where $\mathbf{X}$ is the embedding of the deformed shell in Euclidean

space $\mathbb{R}^3$ and $\hat{\mathbf{N}}$ is the unit normal to the deformed surface. The stretching and bending strains are simply $\varepsilon_{ij} = (\bar{a}_{ij} - a_{ij})/2$ and $C_{ij} = b_{ij} - \bar{b}_{ij}$, which when linearized after eliminating the shear strains, reduce to

$$\varepsilon_{ij} = \frac{1}{2}(\nabla_i u_j + \nabla_j u_i) - f b_{ij} \ , \tag{S20}$$

$$C_{ij} = -\nabla_i \nabla_j f + b_{ik} b^k_j f - b_{kj} \nabla_i u^k - b_{ik} \nabla_j u^k - \frac{1}{2} u^k (\nabla_i b_{jk} + \nabla_j b_{ik}) \ . \tag{S21}$$

We note that the raising and lowering of all indices is done with a_{ij}. The usual in-plane stress tensor is $\sigma^{ij} = \mathcal{A}^{ijk\ell}\varepsilon_{ij}$. Upon varying the elastic energy with respect to (u_i, f), we obtain the elastic forces which allows us to write the dynamical equations, i.e., Newton's second law, as

$$\rho h \partial_t^2 \mathbf{u} = -\frac{\delta E}{\delta \mathbf{u}} \ , \tag{S22}$$

$$\rho h \partial_t^2 f = -\frac{\delta E}{\delta f} \ . \tag{S23}$$

For a thin shell, as is relevant to the musical saw (S23), bending deformations are energetically cheaper than stretching. As a result, flexural modes are easily excited and are the primary contributors to the acoustic spectrum. Hence, we consider the in-plane displacements or phonons (u_i) to be in quasistatic equilibrium so that the dominant inertial dynamics arises from the flexural modes (f); this arises due to the dispersive nature of the latter while the in-plane phonon modes are non-dispersive (hyperbolic). We note that in the numerical simulations, the inertial dynamics of the in-plane phonons and the transverse shear are retained as well.

Upon setting $\rho h \partial_t^2 \mathbf{u} \approx \mathbf{0}$, the displacement is simply determined by tangential force balance involving the stress tensor along with additional corrections from the curvature of the shell. Neglecting these higher order terms as $h/R \ll 1$ for a thin shell, where R is the smallest radius of curvature of the reference state, we obtain

$$\frac{\delta E}{\delta u_i} = 0 \implies \nabla_j \sigma^{ij} + \mathcal{O}\left(\frac{Yh^2}{R}\nabla^3 f, \frac{Yh^2}{R^3}\nabla f\right) = 0 \ . \tag{S24}$$

We can solve $\nabla_j \sigma^{ij} = 0$ by a generalization of the Airy stress function for shells, given by

$$\sigma_{ij} = \nabla_i \nabla_j \chi - a_{ij} \frac{1}{\nabla^2} \nabla^k \nabla^2 \partial_k \chi \ , \tag{S25}$$

where $(1/\nabla^2)$ denotes a convolution with the scalar Green's function of the Laplace-Beltrami operator. Note that unlike the planar version of this equation (even for metrically incompatible solids (S24, S25)), this expression is nonlocal due to the noncommutativity of the derivatives. For constant or slowly varying Gaussian curvature ($\partial_i K_G \approx 0$), we can simplify the above expression to a local equation

$$\sigma_{ij} = \nabla_i \nabla_j \chi - a_{ij}(\nabla^2 \chi + K_G \chi) \ . \tag{S26}$$

To obtain this, some useful formulae are $[\nabla_i, \nabla_j] v_k = R^l{}_{kji} v_l$, $[\nabla_i, \nabla_j] M_{kl} = R_{ij}{}^m{}_k M_{ml} + R_{ij}{}^m{}_l M_{km}$, where the reference Riemann curvature tensor $R_{ijkl} = K_G(a_{ik}a_{jl} - a_{il}a_{jk})$ in 2D (K_G being the Gaussian curvature of the reference state) (S26).

In the normal direction, we retain inertial dynamics, which gives

$$\rho h \partial_t^2 f = -\frac{\delta E}{\delta f} = -\frac{h^3}{12} \mathcal{A}^{ijk\ell} \mathcal{L}_{ij} \mathcal{L}_{k\ell} f + \sigma^{ij} b_{ij} \ , \tag{S27}$$

where we have neglected $\mathcal{O}((h/R)^3)$ terms. The differential operator is $\mathcal{L}_{ij} f = \nabla_i \nabla_j f - b_{ik} b^k_j f$ and the elastic tensor $\mathcal{A}^{ijkl}$ is the same as in Eq. S14.

A. Length scales. Let R be the smallest radius of curvature of the reference state, so R^{-1} is the maximum eigenvalue of $\mathbf{b}$ across the whole surface. From Eq. S24 and S20, we can estimate that the relevant strains in the system scale as $\varepsilon_{ij} \sim f/R$. Consequently, the stretching energy scales as $\sim Yf^2/R^2$, while the bending energy scales as $\sim Yh^2 f^2/\ell^4$, where ℓ is the typical length scale of the deformation. Upon balancing the two, we obtain a crossover length scale (S10)

$$\ell_{\rm el} \sim \sqrt{hR} \ll R \ . \tag{S28}$$

Hence on small length scales ($\ell \ll \ell_{\rm el}$), bending dominates while on larger scales ($\ell \gg \ell_{\rm el}$), stretching dominates due to the underlying curvature. Here, in estimating the bending energy, we have neglected terms $\sim b_{ij}^2 \nabla^2 f$ and $\sim b_{ij}^4 f$ that appear in Eq. S27 upon expanding out the operator $\mathcal{L}_{ij}$. One can argue that their neglect is self-consistent in our analysis. For $\ell \ll \ell_{\rm el}$, we have $(\ell/R)^2 \ll h/R \ll 1$, hence

$$\frac{|b_{ij}^2 \nabla^2 f|}{|\nabla^4 f|} \sim \frac{h}{R} \ll 1 \ , \quad \frac{|b_{ij}^4 f|}{|\nabla^4 f|} \sim \left(\frac{h}{R}\right)^2 \ll 1 \ . \tag{S29}$$

Similarly, for $\ell \gg \ell_{\rm el}$, the $\sigma^{ij} b_{ij}$ arising from stretching dominates. As $\sigma_{ij} \sim Y\varepsilon_{ij} \sim Yf/R$, we can once again show that the above terms are negligible in comparison.

$$\frac{|Yh^2 b_{ij}^2 \nabla^2 f|}{|\sigma_{ij} b^{ij}|} \sim \left(\frac{h}{\ell}\right)^2 \ll 1 \ , \quad \frac{|b_{ij}^4 f|}{|\sigma_{ij} b^{ij}|} \sim \left(\frac{h}{R}\right)^2 \ll 1 \ . \tag{S30}$$

In a similar fashion, one can show that the neglected terms in Eq. S24 are $\sim (h/\ell)^2$ and $\sim (h/R)^2$ and hence negligible compared to the terms retained. Hence, for deformations on practically all macroscopic length scales ($\ell \gg h$), the following simplified equations are sufficient to describe the mechanics of thin shells.

$$\nabla_j \sigma^{ij} = 0 \ , \quad \rho h \partial_t^2 f = -\kappa \nabla^2 \nabla^2 f + \sigma^{ij} b_{ij} \ , \tag{S31}$$

where $\kappa = Yh^3/[12(1-\nu^2)]$ is the bending rigidity.

B. Shallow shell theory. To simplify things further, we approximate $a_{ij} \approx \delta_{ij}$ and $\nabla_i \approx \partial_i$ to lowest order, while retaining a constant (or weakly varying) non-zero b_{ij} as is typical of shallow shell theory (S11, S22). This also allows us to disregard any difference between covariant and contravariant indices, thereby greatly simplifying both Eqs. S24 and S27 to give

$$\partial_j \sigma_{ij} = 0 \ , \quad \text{and} \quad \rho h \partial_t^2 f = -\kappa \nabla^4 f + \sigma_{ij} b_{ij} \ , \tag{S32}$$

The stress tensor is determined by the Airy stress function $\sigma_{ij} = \epsilon_{ik}\epsilon_{jl}\partial_k \partial_l \chi = \partial_i \partial_j \chi - \delta_{ij} \nabla^2 \chi$ (S10) (ϵ_{ij} is the Levi-Civita symbol), which itself solves

$$\frac{1}{Yh} \nabla^4 \chi = -b_{ij} \mathcal{P}_{ij} \nabla^2 f \ . \tag{S33}$$

The projection operator is defined as $\mathcal{P}_{ij} = \delta_{ij} - (\partial_i \partial_j / \nabla^2)$. Solving for σ_{ij} in favour of f, we obtain a closed dynamical equation for the flexural mode to be

$$\rho h \partial_t^2 f = -\kappa \nabla^4 f - Yh (b_{ij} \mathcal{P}_{ij})^2 f \ . \tag{S34}$$

Fourier transforming freely in both space and time ($\Phi_{\mathbf{q},\omega} = \int \mathrm{d}^2 x \int \mathrm{d}t \, e^{i\omega t - i\mathbf{q}\cdot\mathbf{x}} \Phi(\mathbf{x}, t)$), we obtain the following dispersion relation for the flexural sound modes in a constant curvature shell

$$\omega_\pm(\mathbf{q}) = \pm \sqrt{\frac{\kappa}{\rho h} q^4 + c^2 \left[b_{ij} \mathcal{P}_{ij}(\hat{\mathbf{q}})\right]^2} \ , \tag{S35}$$

where $c = \sqrt{Y/\rho}$ is the speed of sound, $\hat{\mathbf{q}} = \mathbf{q}/q$ ($q = |\mathbf{q}|$) and $\mathcal{P}_{ij}(\hat{\mathbf{q}}) = \delta_{ij} - \hat{q}_i \hat{q}_j$.

Upon diagonalizing the curvature tensor b_{ij}, we can write it in terms of its principal curvature direction $\hat{\mathbf{t}}$ as $\mathbf{b} = b_\parallel \hat{\mathbf{t}} + b_\perp (\mathbf{1} - \hat{\mathbf{t}}\hat{\mathbf{t}})$, where $b_\parallel, b_\perp$ are the principal reference curvatures ($|b_\parallel| > |b_\perp|$). Therefore, the above dispersion relation in Eq. S35 has a spectral gap near $\mathbf{q} = 0$ iff

$$b_{ij} \mathcal{P}_{ij}(\hat{\mathbf{q}}) = b_\parallel + (b_\perp - b_\parallel)(\hat{\mathbf{q}} \cdot \hat{\mathbf{t}})^2 \neq 0 \quad \forall \hat{\mathbf{q}} \ . \tag{S36}$$

For a spherical shell, $b_\parallel = b_\perp = 1/R_0 > 0$ and we have $b_{ij}\mathcal{P}_{ij}(\hat{\mathbf{q}}) = 1/R_0 > 0$. While on a saddle surface with negative Gaussian curvature, $b_\parallel = 1/R_0, b_\perp = -1/R_0$ which gives $b_{ij}\mathcal{P}_{ij}(\hat{\mathbf{q}}) = [2 - (\hat{\mathbf{q}} \cdot \hat{\mathbf{t}})^2]/(2R_0) > 0$ as well. Hence on both the sphere and a symmetric saddle, the acoustic spectrum is gapped everywhere, though it is anisotropic in the latter case (S27). For a developable surface, $\mathbf{b}$ has atleast one vanishing eigenvalue, say $b_\perp = 0$ without loss of generality. As a consequence $b_{ij}\mathcal{P}_{ij}(\hat{\mathbf{q}}) = b_\parallel [1 - (\hat{\mathbf{q}} \cdot \hat{\mathbf{t}})^2]$ which vanishes for $\hat{\mathbf{q}} = \pm \hat{\mathbf{t}}$. Hence, a developable surface has a line along which the spectrum is gapless, and is gapped elsewhere.

As the dynamics of f is inertial and second order in time, we can write it in terms of first order equations by introducing the normal velocity $v = \partial_t f$

$$\partial_t \begin{pmatrix} f \\ v \end{pmatrix} = \begin{pmatrix} 0 & 1 \\ -c^2 \mathcal{D}\mathcal{D}^\dagger & 0 \end{pmatrix} \begin{pmatrix} f \\ v \end{pmatrix} \ , \tag{S37}$$

where $\mathcal{D} = i\sqrt{\kappa/Yh}\,\nabla^2 + b_{ij}\mathcal{P}_{ij}$ and $\dagger$ denotes the Hermitian conjugate. Note, $\sqrt{\kappa/Yh} \propto h$ is independent of the Young's modulus. By writing $\Phi = (f, v)$, we perform a similarity transformation $\Psi = \mathcal{T}\Phi$ to get a Schrödinger-like equation (S28)

$$\frac{i}{c}\partial_t \Psi = \mathcal{H}\Psi \ , \quad \mathcal{H} = \begin{pmatrix} 0 & \mathcal{D}^\dagger \\ \mathcal{D} & 0 \end{pmatrix} \ , \quad \text{with} \quad \mathcal{T} = \begin{pmatrix} c\mathcal{D}^\dagger & 0 \\ 0 & i \end{pmatrix} \ , \tag{S38}$$

with $\mathcal{H}^2 = \mathcal{D}^\dagger \mathcal{D} \mathbf{1} = (\kappa/Yh)\nabla^4 + (b_{ij}\mathcal{P}_{ij})^2$ ($[\mathcal{D}^\dagger, \mathcal{D}] = 0$ only for constant $\mathbf{b}$, but we neglect it for slowly varying curvature as well). Note that, while $\mathcal{H}$ is Hermitian, $\mathcal{D}$ is *not*. Eq. S38 will be our starting point to discuss the topological features. One can also show that a similar matrix, unitarily equivalent to $\mathcal{H}$, also relates the local stress and bending moment to the local tangential and normal forces, reminiscent of the compatibility matrix in isostatic lattices (S29, S30). We leave the detailed exploration of a possible connection to topological floppy modes (S29, S30) for future work and instead focus on dynamics here.

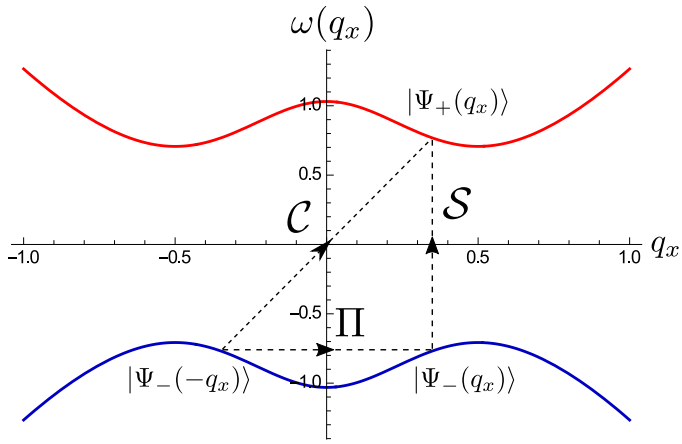

Fig. S5. A plot of the dispersion relation in Eq. S42 for a fixed $q_y \neq 0$. The two bands $|\Psi_\pm\rangle$ respect classical time-reversal symmetry ($\mathcal{S}$), mechanical reciprocity ($\mathcal{C}$) and an effective spatial reflection symmetry (Π). As is evident, the combination of operators $\Pi\mathcal{S}\mathcal{C}^{-1}$ maps the eigenmode to itself, though one may accumulate a phase in doing so. Singularities in this phase result in a nontrivial topological invariant.

C. 1D curved ribbon. Here we shall first work out the details for a developable 1D ribbon curved only along one axis. Without loss of generality, we take $b_\perp = 0$ and $\hat{\mathbf{t}} = \hat{\mathbf{e}}_x$, and set $b_\parallel \equiv b \neq 0$. Upon Fourier transforming in space we obtain

$$\mathcal{D}(\mathbf{q}) \equiv e^{-i\mathbf{q}\cdot\mathbf{x}}\mathcal{D}e^{i\mathbf{q}\cdot\mathbf{x}} = d_x(\mathbf{q}) + id_y(\mathbf{q}) \ , \tag{S39}$$

$$\mathcal{H}(\mathbf{q}) \equiv e^{-i\mathbf{q}\cdot\mathbf{x}}\mathcal{H}e^{i\mathbf{q}\cdot\mathbf{x}} = d_x(\mathbf{q})\boldsymbol{\tau}_x + d_y(\mathbf{q})\boldsymbol{\tau}_y \ , \tag{S40}$$

$$d_x(\mathbf{q}) = b\frac{q_y^2}{q_x^2+q_y^2} \ , \quad d_y(\mathbf{q}) = \sqrt{\frac{\kappa}{Yh}}(q_x^2+q_y^2) \ , \tag{S41}$$

where $\boldsymbol{\tau}_{x,y}$ are Pauli matrices. The eigenvalues and corresponding eigenvectors ($\mathcal{H}|\Psi_\pm\rangle = (\omega_\pm/c)|\Psi_\pm\rangle$, using Dirac's bra-ket notation (S31)) are,

$$\omega_\pm(\mathbf{q}) = \pm c|\mathcal{D}(\mathbf{q})| \ , \quad |\Psi_\pm(\mathbf{q})\rangle = \frac{1}{\sqrt{2}}\begin{pmatrix} 1 \\ \pm e^{i\theta(\mathbf{q})} \end{pmatrix} \ , \tag{S42}$$

with $e^{i\theta(\mathbf{q})} = \mathcal{D}(\mathbf{q})/|\mathcal{D}(\mathbf{q})|$. The eigenvectors are orthonormalized, so $\langle\Psi_m|\Psi_n\rangle = \delta_{mn}$ for $m, n = \pm$. For $q_y = 0$, corresponding to flexural modes that are linearized isometries, the spectrum is gapless with $\omega_\pm \to 0$ as $q_x \to 0$. In contrast, for $q_y \neq 0$, the eigenmodes couple bending and stretching via the curvature of the ribbon leading to a finite band gap $\sim c|b|$, even when $q_x \to 0$. We shall fix $q_y \neq 0$ and look at the effective model only in 1D as a function of q_x (and suppress the q_y dependence hereafter). Note the absence of the third Pauli matrix in Eq. S40 ($\boldsymbol{\tau}_z$ in this basis), that is a consequence of classical time-reversal symmetry (as explained below). We now discuss in detail the various symmetries in the problem, including time reversal, that are crucial for the topological characterization.

***C.1.* Symmetries.** There are three primary symmetries of relevance to us. Note, here we will always assume a fixed $q_y \neq 0$ and describe only the effective 1D symmetries of the system that are relevant to us. To understand the action of any symmetry operation, we recount the eigenvalue problem

$$\mathcal{H}|\Psi_n\rangle = \frac{\omega_n}{c}|\Psi_n\rangle \ , \tag{S43}$$

where $n = \pm$ in our specific two band case. The sound speed $c > 0$ is a constant and simply scales the eigenfrequencies ω_n. For the purposes of the symmetry analysis below, we can rescale ω_n and set $c = 1$ without loss of generality. The eigenfunctions are orthonormal, $\langle\Psi_n|\Psi_m\rangle = \delta_{nm}$, which allows us to freely rotate each eigenfunction by an arbitrary complex phase ($|\Psi_n\rangle \to e^{i\varphi_n}|\Psi_n\rangle$) that leaves both the normalization and Eq. S43 unchanged. While the absolute phase is a gauge freedom and is not observable, relative differences in the phase are observable and important.

The first symmetry is a consequence of classical time reversal in Newtonian mechanics, that leads to a redundancy in the description (S28, S29). Time reversal alone forces all the eigenvalues of $\mathcal{H}$ appear in $\pm$ pairs (and the eigenmodes $|\Psi_\pm\rangle$, being time-reversal even, map onto themselves upon flipping time). As a result, we interchange the $\omega > 0$ bands with the $\omega < 0$ ones, i.e., forward moving waves become backward moving waves and vice-versa. This is implemented using a unitary operator $\mathcal{S}$

$$\mathcal{S}\mathcal{H}(q_x)\mathcal{S}^{-1} = -\mathcal{H}(q_x) \ , \quad \mathcal{S} = \boldsymbol{\tau}_z \ , \tag{S44}$$

where the final expression for $\mathcal{S}$ ($\mathcal{S}^2 = \mathbf{1}$) is written in the same basis for which $\mathcal{H}$ adopts the form in Eqs. S38, S40. Note that, the symmetry operation performed by $\mathcal{S}$, while being a consequence of *classical* time-reversal, it is distinct from (and unrelated to) the time-reversal symmetry operation used in the quantum mechanical context, where instead $\mathcal{S}$ would refer to what's called a "chiral" or "sublattice" symmetry.

We can easily check the the operator $\mathcal{S}$ actually implements classical time-reversal, as follows

$$\begin{aligned} \mathcal{S}\mathcal{H}(q_x)\mathcal{S}^{-1}\mathcal{S}|\Psi_n(q_x)\rangle &= \omega_n(q_x)\mathcal{S}|\Psi_n(q_x)\rangle \\ \implies \mathcal{H}(q_x)\mathcal{S}|\Psi_n(q_x)\rangle &= -\omega_n(q_x)\mathcal{S}|\Psi_n(q_x)\rangle \\ &= \omega_{-n}(q_x)\mathcal{S}|\Psi_n(q_x)\rangle \ . \end{aligned} \tag{S45}$$

Here we have employed the fact that bands come in pairs with opposite sign eigenvalues, therefore $\omega_n(q_x) = -\omega_{-n}(q_x)$, where we have used the convention of labelling the $\omega > 0$ bands with positive integers and the $\omega < 0$ bands with negative integers.

The second symmetry is related to time-reversal again, but is distinct. It has to do with the absence of nonreciprocal or active elements in the material (i.e., no Coriolis force, no magnetic field, no nonconservative interactions) that would generally generate a velocity dependent force. As the underlying degrees of freedom (flexural deflections) and the dynamical matrix are purely real, the eigenmodes with opposite sign eigenvalues are additionally related to each other by complex conjugation. This operation is implemented using an *antiunitary* operator (as it involves complex conjugation) $\mathcal{C}$

$$\mathcal{C}\mathcal{H}(q_x)\mathcal{C}^{-1} = -\mathcal{H}(-q_x) \ , \quad \mathcal{C} = i\boldsymbol{\tau}_y K \ , \tag{S46}$$

where the final expression for $\mathcal{C}$ ($\mathcal{C}^2 = -\mathbf{1}$) is once again in the same basis as chosen to represent $\mathcal{H}$ in Eqs. S38, S40. K is the (antiunitary) complex conjugation operator ($KiK^{-1} = -i$, $K^2 = 1$), and by convention, it also flips the sign of q_x (i.e., $Kq_xK^{-1} = -q_x$). This latter property is to allow K and ∂_x to commute in real space. Here, the operator $\mathcal{C}$ implements the analog of a "particle-hole" symmetry (in the context of superconductors). Note that, both these symmetries ($\mathcal{C}, \mathcal{S}$) are generically present for any time-reversal invariant reciprocal mechanical system, as a result of which the low frequency dynamics in 1D for such systems lies in the BDI class (S28, S32, S33). The appropriate topological classification in this category involves the fundamental group $\pi_1(S^1) = \mathbb{Z}$, with the most well-known example being the Su-Schrieffer-Heeger (SSH) model (S34) and its mechanical analog (S29). We will return to this point later.

The action of the operator $\mathcal{C}$ relates the different eigenmodes within the (classical) time-reversal pair through complex conjugation as follows,

$$\begin{aligned} \mathcal{C}\mathcal{H}(q_x)\mathcal{C}^{-1}\mathcal{C}|\Psi_n(q_x)\rangle &= \mathcal{C}\omega_n(q_x)|\Psi_n(q_x)\rangle \\ \implies \mathcal{H}(-q_x)\mathcal{C}|\Psi_n(q_x)\rangle &= \omega_{-n}(-q_x)\mathcal{C}|\Psi_n(q_x)\rangle \\ \implies \mathcal{H}(q_x)\mathcal{C}|\Psi_{-n}(-q_x)\rangle &= \omega_n(q_x)\mathcal{C}|\Psi_{-n}(-q_x)\rangle \ , \end{aligned} \tag{S47}$$

where we have kept track of the fact that K (and hence $\mathcal{C}$) also flips the sign of q_x.

In addition to the above two ubiquitous *dynamic* symmetries in inertial, passive, elastic media, there is also a *spatial* symmetry that arises from the geometry of the thin shell. It is an effective spatial reflection symmetry $q_x \to -q_x$ for a uniaxially curved shell. This is due to the fact that the normal force from bending only involves an even number of gradients on $\nabla^2 f$, which in turn is a consequence of 3D rotational invariance (as uniform tilts, corresponding to linearized 3D rotations, must leave the energy invariant). This fundamental requirement manifests as an emergent spatial reflection symmetry of $x \to -x$ ($q_x \to -q_x$) within the local tangent plane at a point on the shell. Note that this is a *local* and not a *global* symmetry requirement, a point we test in the simulations by using asymmetric boundary conditions (see Fig. S2). We implement this spatial symmetry within the local tangent plane using a unitary operator Π,

$$\Pi\mathcal{H}(q_x)\Pi^{-1} = \mathcal{H}(-q_x) \ , \tag{S48}$$

with $\Pi^2 = \mathbf{1}$. For our current problem, the representation of $\mathcal{H}$ from Eq. S40 makes $\Pi = \mathbf{1}$ explicitly trivial, as $\mathcal{H}(q_x) = \mathcal{H}(-q_x)$.

The action of the reflection symmetry operator Π is simpler as it relates the same eigenmode for opposite sign wavevectors (q_x) in the following fashion,

$$\begin{aligned} \Pi\mathcal{H}(q_x)\Pi^{-1}\Pi|\Psi_n(q_x)\rangle &= \Pi\omega_n(-q_x)|\Psi_n(q_x)\rangle \\ \implies \mathcal{H}(-q_x)\Pi|\Psi_n(q_x)\rangle &= \omega_n(-q_x)\Pi|\Psi_n(q_x)\rangle \\ \implies \mathcal{H}(q_x)\Pi|\Psi_n(-q_x)\rangle &= \omega_n(q_x)\Pi|\Psi_n(-q_x)\rangle \ . \end{aligned} \tag{S49}$$

Hence, Eqs. S45, S47 and S49 show that the symmetry operators ($\mathcal{C}$, $\mathcal{S}$, $\mathcal{P}$) provide two separate ways of relating $|\Psi_+(q_x)\rangle$ to $|\Psi_-(q_x)\rangle$ (see Fig. S5). When applied in a cyclic fashion, for example with the combination $\Pi\mathcal{S}\mathcal{C}^{-1}$, one can map each eigenmode back to itself, though up to a net phase that doesn't change the eigenmode normalization. If this phase hosts a winding singularity as a function of q_x, then the band structure is topologically nontrivial. Below, we explain how to construct the topological invariant that captures such a phase singularity and compute it for the geometry of a singing saw.

C.2. **$\mathbb{Z}_2$ Topological invariant.** Before we formulate the new $\mathbb{Z}_2$ topological invariant, we first demonstrate how the presence of spatial reflection symmetry (Π) trivializes the Kane-Lubensky polarization or winding number present in Newtonian elastic systems respecting time-reversal symmetry (S29). Classical time-reversal (implemented by $\mathcal{S}$) can be used to always bring the Hermitian dynamical matrix $\mathcal{H}$ into the form of Eq. S40, where the vector $\mathbf{d}(q_x) = (d_x(q_x), d_y(q_x))$ (or conversely the complex number $\mathcal{D}(q_x) = d_x(q_x) + id_y(q_x)$) is always nonvanishing and restricted to a plane. As $|\mathbf{d}(q_x)| \neq 0$ ($|\mathcal{D}(q_x)| \neq 0$) for any q_x (due to the presence of a finite spectral gap), we can ask how many times $\hat{\mathbf{d}} = \mathbf{d}/|\mathbf{d}| \in S^1$ winds around the origin. The same

holds true if working with the entirely equivalent complex number $\mathcal{D}(q_x)$ instead of the vector $\mathbf{d}$. Upon compactifying the real line ($q_x \in \mathbb{R}$) to S^1, the equivalence classes of the map $\hat{\mathbf{d}} : S^1 \to S^1$ are classified by the fundamental group $\pi_1(S^1) = \mathbb{Z}$. This integer winding number (denoted here by n_{KL}) is the standard Kane-Lubensky polarization (S29, S30, S35).

One can easily use the spatial reflection symmetry to show that this integer winding number (n_{KL}) vanishes identically in our system. The proof uses the fact that $\mathcal{D}(q_x) = \mathcal{D}(-q_x)$ (Eqs. S39, S41) which gives

$$n_{KL} = \int_{-\infty}^{\infty} \frac{\mathrm{d}q_x}{2\pi i} \partial_{q_x} \ln(\mathcal{D}(q_x)) = \int_{-\infty}^{\infty} \frac{\mathrm{d}q_x}{2\pi i} \partial_{-q_x} \ln(\mathcal{D}(q_x)) = -n_{KL} \ . \tag{S50}$$

Hence $n_{KL} = 0$ and the curved ribbon is *not* topologically polarized like the SSH model (S29). Note, the existence of n_{KL} only requires a gapped spectrum for a (classically) time-reversal symmetric system. The vanishing winding index then allows us to freely make a globally consistent and smooth choice of the phase, in a time-reversal symmetric fashion, for the eigenmodes over all q_x.

But a vibrating uniaxially curved shell has additional fundamental, particularly spatial, symmetries that are equally important. Unlike the SSH model, the shell has more restrictions imposed by the symmetry operators $\mathcal{C}, \mathcal{S}, \Pi$ on the structure of its eigenmodes, and small variations or disorder in the shape of the shell or its material properties do not violate these basic symmetries. The question then is, can we always find a consistent and smooth choice of the eigenvector phase everywhere in q_x space, so that it respects *all* the dynamic and spatial symmetries of the problem? If such a choice does not exist, only then is the system said to be topologically nontrivial. As we show later, spatial reflection symmetry (in the tangent plane) admits a new symmetry protected topological invariant that causes the $\mathbb{Z}$ classification (by n_{KL}) to collapse to a $\mathbb{Z}_2$ classification instead. While the bending energy is locally symmetric under in-plane reflections of the tangent plane ($\partial_x \to -\partial_x$), to retain a fixed handedness of the frame $\{\mathbf{e}_x, \mathbf{e}_y, \hat{\mathbf{n}}\}$, one must reverse the sign of the unit normal as well ($\hat{\mathbf{n}} \to -\hat{\mathbf{n}}$). The reference curvature breaks up-down inversion symmetry and poses a new obstruction to smoothly defining symmetry respecting eigenfunctions everywhere, and is quantified by a novel $\mathbb{Z}_2$ topological invariant.

We shall first construct the $\mathbb{Z}_2$ topological invariant generally and then specialize it to the shell model at hand. From Eqs. S47, S45 and S49 we know that $|\Psi_n(q_x)\rangle$ and $|\Psi_{-n}(q_x)\rangle$ are directly related (up to a phase) in two different ways. The first is through a combination of reciprocity ($\mathcal{C}$) and reflection symmetry (Π), which gives

$$|\Psi_n(q_x)\rangle = e^{i\chi_n(q_x)} \mathcal{C}\Pi |\Psi_{-n}(q_x)\rangle \ , \tag{S51}$$

where $\chi_n(q_x)$ is an arbitrary phase that represents the free gauge choice for the eigenvector. Alternately, (classical) time-reversal alone ($\mathcal{S}$), also relates the same two eigenmodes, though with a different arbitrary phase $\tilde{\chi}_n(q_x)$,

$$|\Psi_n(q_x)\rangle = e^{i\tilde{\chi}_n(q_x)} \mathcal{S} |\Psi_{-n}(q_x)\rangle \ . \tag{S52}$$

The fact that the time-reversal invariant polarization $n_{KL} = 0$, implies that we can always set $\tilde{\chi}_n(q_x) = 0$ everywhere, but this does *not* guarantee that $\chi_n(q_x)$ vanishes everywhere. The latter, importantly, involves both spatial and dynamic symmetries that are crucial to the saw. The $\mathbb{Z}_2$ invariant we compute represents an obstruction to setting *both* $\chi_n(q_x) = 0$ *and* $\tilde{\chi}_n(q_x) = 0$ for all q_x.

A convenient way to extract these phases $(\chi_n, \tilde{\chi}_n)$ is through the following overlap or "sewing" matrices (S36)

$$T_{mn} = \langle \Psi_m(q_x) | \mathcal{S} | \Psi_n(q_x) \rangle = \delta_{n+m,0} \ e^{i\tilde{\chi}_n(q_x)} \ , \tag{S53}$$

$$W_{mn} = \langle \Psi_m(q_x) | \mathcal{C}\Pi | \Psi_n(q_x) \rangle = \delta_{n+m,0} \ e^{-i\chi_n(q_x)} \ . \tag{S54}$$

As $\mathcal{S}^2 = \mathbf{1}$, $\mathbf{T}$ is traceless unitary matrix ($|\det(\mathbf{T})| = 1$), with $\tilde{\chi}_{-n}(q_x) = -\tilde{\chi}_n(q_x)$ (from Eq. S52). By using the fact that $[\mathcal{C}, \Pi] = \mathbf{0}$ and $\mathcal{C}^2 = -\mathbf{1}$, one can show that $\mathbf{W}^T = -\mathbf{W}$ ($|\det(\mathbf{W})| = 1$), with $e^{i\chi_{-n}(q_x)} = -e^{i\chi_n(q_x)}$ (Eq. S51). For the two-band case, $m, n = \pm$ and we have ($\tilde{\chi}_- \equiv \tilde{\chi}$, $\chi_- \equiv \chi$)

$$\mathbf{T}(q_x) = \begin{pmatrix} 0 & e^{i\tilde{\chi}(q_x)} \\ e^{-i\tilde{\chi}(q_x)} & 0 \end{pmatrix} \ , \quad \mathbf{W}(q_x) = \begin{pmatrix} 0 & e^{-i\chi(q_x)} \\ -e^{-i\chi(q_x)} & 0 \end{pmatrix} \ . \tag{S55}$$

As $n_{KL} = 0$, we can always choose a gauge that makes $\mathbf{T}$ a constant matrix (for $\tilde{\chi} = 0$, $\mathbf{T} = \boldsymbol{\tau}_x$). This is the basis we shall work in.

To construct the topological invariant, we start with the Berry connection (which is essentially like the spin-connection on a surface (S37), only now in Fourier space)

$$\mathcal{A}_n(q_x) = \langle \Psi_n(q_x) | i\partial_{q_x} | \Psi_n(q_x) \rangle \ . \tag{S56}$$

As expected, a phase transformation $|\Psi_n(q_x)\rangle \to e^{i\varphi_n(q_x)} |\Psi_n(q_x)\rangle$ leads to a gauge transformation of the connection $\mathcal{A}_n(q_x) \to \mathcal{A}_n(q_x) - \partial_{q_x}\varphi_n(q_x)$. The topological index is computed using a line integral of $\mathcal{A}_n$ over all q_x,

$$\nu_n = \int_{-\infty}^{\infty} \frac{\mathrm{d}q_x}{\pi} \mathcal{A}_n(q_x) \ . \tag{S57}$$

The factor of π in the denominator is due to reflection symmetry (allowing us to work with integers rather than half-integers). In the following we shall restrict ourselves to the two-band system for simplicity, but the generalization to more bands is straightforward. Upon writing $n = \pm$ now, we have ($\nu_- \equiv \nu$)

$$\nu = \int_{-\infty}^{\infty} \frac{\mathrm{d}q_x}{\pi} \mathcal{A}_-(q_x) = \int_0^{\infty} \frac{\mathrm{d}q_x}{\pi} \left[\mathcal{A}_-(q_x) + \mathcal{A}_-(-q_x)\right] \ . \tag{S58}$$

Now, using Eq. S51 along with the fact that $\partial_{q_x}\mathcal{C} = -\mathcal{C}\partial_{q_x}$ and $[\mathcal{C}, \Pi] = \mathbf{0}$, we find

$$\mathcal{A}_+(q_x) = \mathcal{A}_-(-q_x) - \partial_{q_x}\chi(q_x) \ . \tag{S59}$$

So Eq. S58 simplifies to give,

$$\nu = \int_0^{\infty} \frac{\mathrm{d}q_x}{\pi} \mathcal{A}(q_x) + \frac{[\chi(\infty) - \chi(0)]}{\pi} \ , \tag{S60}$$

where $\mathcal{A}(q_x) = \mathcal{A}_+(q_x) + \mathcal{A}_-(q_x)$. One can repeat the same calculation starting with $\mathcal{A}_+$ as well and we get the same result as above, upon identifying $q_x = \pm\infty$ to compactify Fourier space. Note that, differences in the phase χ are only consequential mod 2π and one can show that the invariant $\nu \in \mathbb{Z}$ mod 2, i.e., only the parity (odd or even) of ν matters. Hence it is more convenient to work with $(-1)^\nu \in \mathbb{Z}_2$ as the relevant topological invariant, which explicitly keeps track of only the parity of ν.

In order to massage the index in Eq. S58 into a more concise form, we use the sewing matrix $\mathbf{W}(q_x)$ introduced above (Eqs. S54, S55). Using the fact that $\mathbf{W}^T = -\mathbf{W}$ and hence $|\det(\mathbf{W})| = 1$, we can easily write

$$\partial_{q_x} \ln\left[\det(\mathbf{W})\right] = \mathrm{tr}\left[\mathbf{W}^\dagger \partial_{q_x}\mathbf{W}\right] = -2\sum_{n=\pm} \langle \Psi_n(q_x)|\partial_{q_x}|\Psi_n(q_x)\rangle \ . \tag{S61}$$

So we find that $\mathcal{A}(q_x) = -i\partial_{q_x} \ln\sqrt{[\det(\mathbf{W})]}$, with the principal branch chosen for the square root of the logarithm. By virtue of being antisymmeric, the Pfaffian of $\mathbf{W}$ is well defined ($\mathrm{Pf}\left[\mathbf{W}(q_x)\right] = e^{-i\chi(q_x)}$ in the two band case, Eq. S55) and is related to the determinant as $\det(\mathbf{W}) = \mathrm{Pf}^2(\mathbf{W})$. This allows us to write

$$\frac{\mathrm{Pf}\left[\mathbf{W}(\infty)\right]}{\mathrm{Pf}\left[\mathbf{W}(0)\right]} = e^{i[\chi(0)-\chi(\infty)]} \ . \tag{S62}$$

Upon using the relation between $\mathcal{A}$ and the log-determinant of $\mathbf{W}$, we can reduce the final integral in Eq. S58 to a simple determinant evaluation at $q_x = 0$ and $q_x = \infty$. Putting it all together we then obtain

$$(-1)^\nu \equiv e^{i\pi\nu} = \exp\left[i\int_0^{\infty} \mathrm{d}q_x\, \mathcal{A}(q_x)\right] \frac{\mathrm{Pf}\left[\mathbf{W}(0)\right]}{\mathrm{Pf}\left[\mathbf{W}(\infty)\right]} = \frac{\mathrm{Pf}\left[\mathbf{W}(0)\right]}{\sqrt{\det\left[\mathbf{W}(0)\right]}} \frac{\sqrt{\det\left[\mathbf{W}(\infty)\right]}}{\mathrm{Pf}\left[\mathbf{W}(\infty)\right]} \in \mathbb{Z}_2 \ . \tag{S63}$$

This completes the derivation of the required $\mathbb{Z}_2$ topological index. Note that our calculation is similar to topological indices employed in inversion symmetric topological insulators (S38, S39) and superconductors (S40), and general topological crystalline insulators (S41, S42).

Unlike conventional electronic topological insulators (S36, S43) or mechanical lattices (S29, S30), that have a closed and finite Brillouin zone by virtue of discrete periodicity, we are working directly in the continuum and the bulk invariant in Eq. S63 explictly depends on the behaviour of the shell model at short distances ($q_x \to \pm\infty$). On scales smaller than the thickness of the shell ($h|q_x| \gg 1$), the system is no longer well-described as a slender object and the material responds as an isotropic 3D elastic body. On these scales, the material microstructure will become important and the macroscopic curvature of the shell is irrelevant. In order to construct a topological invariant that is *independent* of the details of microscopic regularization and only depends on long-wavelength properties of the system, we only consider a *bulk-difference invariant* (S44), which quantifies the net change in the topological invariant across an interface between two different bulk systems that are in contact. This is essentially the same strategy also used to analyze topological modes in continuum fluids (S45–S48).

Denoting the two separate systems (in the musical saw, these would be the two oppositely curved parts of the blade) using $\mathcal{H}_<$ and $\mathcal{H}_>$, we shall assume that the microscopic behaviour at $|q_x| = \infty$ is the same in both systems, i.e.,

$$\lim_{|q_x|\to\infty} \mathcal{H}_<(q_x) = \lim_{|q_x|\to\infty} \mathcal{H}_>(q_x) \ . \tag{S64}$$

This is appropriate for the saw, as the material is identical on either side of the inflection point, the only difference is in the macroscopic geometry. The corresponding Fourier spaces associated with each of the two bulk segments are denoted by $\mathcal{I}_<$ and $\mathcal{I}_>$ respectively. Eq. S64 allows us to combine the two spaces into a compact manifold $\mathcal{I}$ by identifying the points at infinity (S44),

$$\mathcal{I} = \mathcal{I}_< \cup \mathcal{I}_>/(\infty_< \sim \infty_>) \cong S^1 \ , \tag{S65}$$

where the equivalence relation ($\infty_< \sim \infty_>$) denotes the identification of the points $q_x = \pm\infty$ in $\mathcal{I}_<$ to the corresponding $q_x = \pm\infty$ in $\mathcal{I}_>$. As a now have a closed and compact manifold ($\mathcal{I} \cong S^1$), we can use the same construction as before to now derive the *bulk-difference inavariant*

$$(-1)^{\Delta\nu} = \frac{\mathrm{Pf}\left[\mathbf{W}_<(0)\right]}{\sqrt{\det\left[\mathbf{W}_<(0)\right]}} \frac{\sqrt{\det\left[\mathbf{W}_>(0)\right]}}{\mathrm{Pf}\left[\mathbf{W}_>(0)\right]} \in \mathbb{Z}_2 \ , \tag{S66}$$

which quantifies change in the topological index ($\Delta\nu$) across the interface. As is clear from the expression, $\Delta\nu$ is now explicitly *independent* of the short distance ($|q_x| \to \infty$) details of the model and is a well defined topological index that only relies on the universal large scale properties of the system. When $\Delta\nu = 1 \pmod 2$, the two systems are topologically distinct and the interface hosts a single localized mode that lies within the bulk spectral gap and is protected by the topology of the bulk on either side.

In the context of the musical saw, we now explicitly compute this invariant for a 1D strip that has spatially varying uniaxial curvature b that changes sign across an inflection point. Far from the inflection point, on either side, we can adiabatically deform the system to have constant curvature (though the sign will be different on either side of the inflection point) without hitting any singularities in the spectrum or band structure (as the spectrum is always gapped as long as $|b| > 0$). This allows us to use the bulk description of a constant curvature shell away from the inflection, and we denote the curvature on either side as $b_<$ and $b_>$. Upon using the explicit expressions of the eigenmodes in Eq. S42, we can compute the overlap or sewing matrices $\mathbf{T}$ and $\mathbf{W}$ (Eq. S55) as

$$\mathbf{T}(q_x) = \begin{pmatrix} 0 & 1 \\ 1 & 0 \end{pmatrix} , \quad \mathbf{W}(q_x) = \begin{pmatrix} 0 & -e^{-i\theta(q_x)} \\ e^{-i\theta(q_x)} & 0 \end{pmatrix} . \tag{S67}$$

The eigenmodes $|\Psi_\pm\rangle$ in Eq. S42 are already in a convenient representation as $\tilde{\chi}(q_x) = 0$. $\mathbf{W}$ on the other hand, remains nontrivial, with $\chi(q_x) = \theta(q_x) + \pi \pmod{2\pi}$, where $e^{i\theta(q_x)} = \mathcal{D}(q_x)/|\mathcal{D}(q_x)|$. As $\mathcal{D}(0) = i\sqrt{\kappa/Yh}q_y^2 + b$, $\mathrm{Pf}[\mathbf{W}(0)] = (-b + i\sqrt{\kappa/Yh}q_y^2)/|\mathcal{D}(0)|$ has an acute argument ($< \pi/2$) when $b < 0$, and an obtuse argument ($> \pi/2$) when $b > 0$. Upon using the principal branch for the square root of the determinant, we obtain

$$\frac{\mathrm{Pf}[\mathbf{W}(0)]}{\sqrt{\det[\mathbf{W}(0)]}} = -\mathrm{sgn}(b) . \tag{S68}$$

From Eq. S66, the change in the $\mathbb{Z}_2$ invariant across an interface straddling two regions with curvature $b_<$ and $b_>$ is simply

$$(-1)^{\Delta\nu} = \mathrm{sgn}\left(b_< b_>\right) . \tag{S69}$$

Hence when the curvature changes sign across the interface/inflection point, we are guaranteed to find a topologically protected mode within the bulk band gap, localized right at the interface. While our current calculation relied on uniaxial curvature and an essentially 1D geometry, extensions to 2D with surfaces curved in two directions are possible and left for future work.

D. Interface localized mode. Here we compute the profile of the interfacially localized midgap state. We first choose a simple linear curvature profile with $b(x) = b'x$, with a constant curvature gradient b' and an inflection point at the origin ($x = 0$), as done in Ref. (S23). Upon Fourier transforming in time and the transverse (y) direction, and assuming slow variations in the x-direction ($\partial_x^2 \ll q_y^2$ and $\mathcal{P}_{xx} \simeq 1$), we have to leading order in gradients

$$-\rho h\omega^2 f(x) = 2\kappa q_y^2 \partial_x^2 f(x) - [\kappa q_y^4 + Yh(b')^2 x^2] f(x) , \tag{S70}$$

which is nothing but the equation for a quantum simple harmonic oscillator (S31). The lowest localized mode is given by the ground state, which is a Gaussian $f(x) \sim e^{-x^2/2\xi^2}$ The localization length ξ and corresponding mode frequency ω_0 (the time-reversal partner of the localized mode has frequency $-\omega_0$) is given by

$$\xi = \left(\frac{2\kappa}{Yh}\right)^{1/4} \sqrt{\left|\frac{q_y}{b'}\right|} \propto \left(\frac{h|q_y|}{|b'|}\right)^{1/2} , \tag{S71}$$

$$\omega_0(q_y)^2 = |q_y| \frac{\kappa}{\rho h} \left[|b'| \sqrt{\frac{2Yh}{\kappa}} + |q_y|^3 \right] \sim c^2 h |q_y b'| \quad (q_y \to 0) , \tag{S72}$$

where the final limit of $q_y \to 0$ is only approximate and cannot be reached as the bulk gap vanishes when $q_y = 0$ and no localized mode exists then. Nonetheless, it is clear that the topologically localized mode has a dispersive spectrum controlled by the curvature profile of the shell. Strong localization is achieved when $\xi/L \ll 1$ (L is the length of the saw), which implies

$$\frac{L|b'|}{|q_y|} \gg \frac{h}{L} . \tag{S73}$$

Hence large variations in curvature and small transverse mode numbers (q_y, but still large enough so that we can assume $\partial_x^2 \ll q_y^2$) lead to the well localized modes as confirmed by our full numerical simulations as well (Fig. 2D-E). One can also perform the same calculation for a tanh curvature profile $b(x) = b_0 \tanh(x/\ell)$ that smoothly interpolates between two constant curvature sections of the strip. This is related to yet another quantum mechanics problem, now in a Pöschl-Teller potential (S31),

$$-\rho h\omega^2 f(x) = 2\kappa q_y^2 \partial_x^2 f(x) - \left[\kappa q_y^4 + Yh b_0^2 \tanh^2\left(\frac{x}{\ell}\right)\right] f(x) . \tag{S74}$$

The effective potential depth is $V_0 = Yh\ell^2 b_0^2/(4\kappa q_y^2) \sim (\ell/h)^2 (W/R)^2 \gtrsim 1$, where $|b_0| \sim 1/R$ and $|q_y| \sim 1/W$. The ground state eigenmode is given in terms of Legendre functions, $f(x) \sim P_\lambda^\lambda(\tanh(x/\ell)) \propto (1 - \tanh^2(x/\ell))^{\lambda/2}$ where $\lambda = \lfloor(\sqrt{1 + 8V_0} - 1)/2\rfloor$

(the integer part) with the localization length $\xi \sim \ell/\sqrt{\lambda} \propto (h\ell|q_y/b_0|)^{1/2}$ for large V_0, which is the same scaling as in Eq. S71, with the gradient $b' = b_0/\ell$ evaluated at the origin. The frequency of the localized mode (for $V_0 \gtrsim 1$) is

$$\omega_0(q_y)^2 = \frac{\kappa}{\rho h} q_y^4 + c^2 b_0^2 - \frac{2\kappa q_y^2}{\rho h \ell^2}\lambda^2 \simeq |q_y| \frac{\kappa}{\rho h}\left[\frac{|b_0|}{\ell}\sqrt{\frac{2Yh}{\kappa}} + |q_y|^3\right] , \tag{S75}$$

which is also the same dispersive scaling as in Eq. S72, with the curvature gradient evaluated at the origin ($b' = b_0/\ell$). Notably though, we see that the localized mode with $\lambda > 0$ has a frequency that lies within the bandgap of the bulk (the finite q_y frequency gap for constant curvature b_0 is $\sqrt{(\kappa/\rho h)q_y^4 + c^2 b_0^2}$), as expected. For arbitrary curvature profiles, we only have to focus on its zeros, each of which will host a topologically protected mode that lies within the bulk band gap and is well-localized for a thin enough shell (Eq. S73). The mode frequency and its localization length can be tuned easily by varying the spatial gradient of curvature near the inflection point.

E. Weakly nonlinear deformations. Until now, we have focused exclusively on linearized deformations and shown how spatial curvature leads to nontrivial band topology that can induce localization of acoustic modes at inflection points on curved shells. Here we extend our analysis to demonstrate how the topological protection of the localized mode also extends to weakly nonlinear deformations. Elastic systems distinguish themselves from quantum electronic systems in that geometric nonlinearities are inherent to mechanics, and such nonlinear deformations arise from integrating incremental linearized displacements that change the global geometry and structure of the system. A striking example is in 1D mechanical SSH chains, where a nonlinear topological soliton can mediate "conduction" in an otherwise (linearly) "insulating" bulk (S49). Working within shallow shell theory, we now retain nonlinear terms in flexural modes that are the most dominant geometric nonlinearity for weakly nonlinear deformations. This modifies the strain tensor to be (S11, S13)

$$\varepsilon_{ij} = \frac{1}{2}(\partial_i u_j + \partial_j u_i) - b_{ij} f + \frac{1}{2}\partial_i f \partial_j f . \tag{S76}$$

We neglect the nonlinear terms in $\mathbf{u}$ which are subdominant. Force balance $\partial_j \sigma_{ij} = 0$ can still be solved by the Airy stress function χ, which satisfies

$$\frac{1}{Yh}\nabla^4 \chi = -\mathcal{P}_{ij}\nabla^2\left[b_{ij} f - \frac{1}{2}\partial_i f \partial_j f\right] . \tag{S77}$$

The source of stress on the right hand side is essentially proportional to the local Gaussian curvature generated by a deflection f and it now includes a quadratic nonlinearity. The total elastic energy takes a simple form in terms of χ, $E = (1/2)\int \mathrm{d}^2x[\kappa(\nabla^2 f)^2 + (1/Yh)(\nabla^2\chi)^2]$. Upon solving Eq. S77 for χ, we obtain the elastic energy entirely in terms of f to be (S50, S51)

$$E = \frac{1}{2}\int \mathrm{d}^2x \left\{\kappa(\nabla^2 f)^2 + \frac{Yh}{2}\left[\mathcal{P}_{ij}\left(b_{ij} + \frac{1}{2}\partial_i\partial_j f\right) f\right]^2\right\} , \tag{S78}$$

where we have used the fact that $\mathcal{P}_{ij}\partial_i = 0$ to write $\mathcal{P}_{ij}(\partial_i f \partial_j f) = -\mathcal{P}_{ij}(f\partial_i\partial_j f)$. Hence for weakly nonlinear deformations, we see that the effective curvature of the shell gets modified as $b_{ij}^{\text{eff}} = b_{ij} + (1/2)\partial_i\partial_j f$. The localized mode is apprciable only near the inflection point, where $b_{ij} \approx 0$ and is exponentially small away from it. So we focus on the vicinity of the inflection point (which we assume is at $x = 0$). For a uniaxially curved shell with $b_{yy} = 0 = b_{xy}$ and $b_{xx} = b(x)$, the effective curvature generated by the localized mode is

$$b_{xx}^{\text{eff}} \approx b(x) + \frac{1}{2}\partial_x^2 f(0) , \quad b_{yy}^{\text{eff}} \approx -\frac{1}{2}q_y^2 f(0) , \tag{S79}$$

while $b_{xy} \approx 0$ as $\partial_x f(0) = 0$. This can be formalized within perturbation theory in f as well, using which we can show that only the correction to b_{xx} is relevant to leading order, while the other components only affect the dispersion relation at higher order. Importantly, we find that the curvature profile $b(x)$ gets shifted by a nonzero constant $\partial_x^2 f(0) = A_0/\xi^2$, where A_0 is proportional to the amplitude of the deformation. If $b(x)$ has a zero (inflection point) across which the curvature changes sign, then b_{xx}^{eff} continues to host a zero, only with its position shifted. This is easily seen by linearizing $b(x) \approx b'x$ near $x = 0$, for which $b_{xx}^{\text{eff}} \approx b'x + A_0/(2\xi^2)$ and the new inflection point is now at $x = -A_0/(2b'\xi^2)$. As a result, the localized mode survives, but its location simply shifts for nonlinear deformations, highlighting the robustness of the topological mode. In contrast, if the curvature profile $b(x)$ did not change sign across its zero, for instance if $b(x) = b_2 x^2$, then $x = 0$ will host a localized mode due ot an accidental degeneracy that is *not* topologically protected (as both sides of the origin have the same sign of curvature). As a consequence, this mode is unstable to perturbations including weakly nonlinear deformations. The accidental localized mode, when excited, will generate an effective curvature $b_{xx}^{\text{eff}} \approx b(x) + A_0/(2\xi^2)$ that loses its zero and is finite everywhere, thereby gapping the localized mode and destroying it [*]. Hence, topology protects the localized mode at the inflection point from weakly nonlinear deformations as well, allowing it to simply translate the curvature domain wall that engendered it.

[*] The localized mode develops a finite gap when $A_0 b_2 > 0$. If the deflection is such that $A_0 b_2 < 0$, then an even number of inflection points will appear, each of which can host a topologically protected mode. This state is also unstable to large perturbations that can cause the inflection points to merge and annihilate in pairs.

References

[S1] MS Alnæs, et al., The fenics project version 1.5. *Arch. Numer. Softw.* **3** (2015).

[S2] A Logg, KA Mardal, G Wells, *Automated solution of differential equations by the finite element method: The FEniCS book*. (Springer Science & Business Media) Vol. 84, (2012).

[S3] JS Hale, M Brunetti, SPA Bordas, C Maurini, Simple and extensible plate and shell finite element models through automatic code generation tools. *Comput. & Struct.* **209**, 163–181 (2018).

[S4] E Reissner, The effect of transverse shear deformation on the bending of elastic plates. *J. appl. Mech.*, A69–A77 (1945).

[S5] RD Mindlin, Influence of rotatory inertia and shear on flexural motions of isotropic, elastic plates. *J. appl. Mech.* **18**, 31–38 (1951).

[S6] PG Ciarlet, *Theory of Shells*, Mathematical Elasticity. (Elsevier Science), (2000).

[S7] D Chapelle, KJ Bathe, *The Finite Element Analysis of Shells - Fundamentals*. (Springer Berlin Heidelberg), (2011).

[S8] GR Kirchhoff, Über die gleichungen des gleichgewichtes eines elastischen körpers bei nicht unendlich kleinen verschiebungen seiner theile. *Sitzungsberichte der Math. Cl. der Kaiserlichen Akademie der Wissenschaften Wien IX* (1852).

[S9] AEH Love, *A Treatise on the Mathematical Theory of Elasticity*. (University Press), 4 edition, (1927).

[S10] LD Landau, E Lifshitz, *Theory of Elasticity,*. (Elsevier, New York) Vol. 3, p. 109 (1986).

[S11] B Audoly, Y Pomeau, *Elasticity and geometry: from hair curls to the non-linear response of shells*. (Oxford University Press), (2010).

[S12] O Iosifescu, Regularity for naghdi's shell equations. *Math. Mech. Solids* **5**, 453–465 (2000).

[S13] WT Koiter, On the nonlinear theory of thin elastic shells. *Proc. Koninkl. Ned. Akad. van Wetenschappen, Ser. B* **69**, 1–54 (1966).

[S14] E Efrati, E Sharon, R Kupferman, Elastic theory of unconstrained non-euclidean plates. *J. Mech. Phys. Solids* **57**, 762–775 (2009).

[S15] Y Klein, E Efrati, E Sharon, Shaping of elastic sheets by prescription of non-euclidean metrics. *Science* **315**, 1116–1120 (2007).

[S16] D Arnold, F Brezzi, Locking-free finite element methods for shells. *Math. Comput. Am. Math. Soc.* **66**, 1–14 (1997).

[S17] D Chapelle, Some new results and current challenges in the finite element analysis of shells. *Acta Numer.* **10**, 215–250 (2001).

[S18] JH Bramble, T Sun, A locking-free finite element method for naghdi shells. *J. Comput. Appl. Math.* **89**, 119–133 (1998).

[S19] NM Newmark, A method of computation for structural dynamics. *J. engineering mechanics division* **85**, 67–94 (1959).

[S20] C Kane, JE Marsden, M Ortiz, M West, Variational integrators and the newmark algorithm for conservative and dissipative mechanical systems. *Int. J. for numerical methods engineering* **49**, 1295–1325 (2000).

[S21] V Hernandez, JE Roman, V Vidal, Slepc: A scalable and flexible toolkit for the solution of eigenvalue problems. *ACM Transactions on Math. Softw. (TOMS)* **31**, 351–362 (2005).

[S22] PG Ciarlet, *Mathematical Elasticity: Volume III: Theory of Shells*. (North-Holland), (2000).

[S23] J Scott, JH Woodhouse, Vibration of an elastic strip with varying curvature. *Philos. Transactions Royal Soc. London. Ser. A: Phys. Eng. Sci.* **339**, 587–625 (1992).

[S24] M Moshe, E Sharon, R Kupferman, The plane stress state of residually stressed bodies: A stress function approach. *arXiv preprint arXiv:1409.6594* (2014).

[S25] M Moshe, I Levin, H Aharoni, R Kupferman, E Sharon, Geometry and mechanics of two-dimensional defects in amorphous materials. *Proc. Natl. Acad. Sci.* **112**, 10873–10878 (2015).

[S26] MPd Carmo, *Riemannian geometry*. (Birkhäuser), (1992).

[S27] AA Evans, AJ Levine, Reflection and refraction of flexural waves at geometric boundaries. *Phys. review letters* **111**, 038101 (2013).

[S28] R Süsstrunk, SD Huber, Classification of topological phonons in linear mechanical metamaterials. *Proc. Natl. Acad. Sci.* **113**, E4767–E4775 (2016).

[S29] C Kane, T Lubensky, Topological boundary modes in isostatic lattices. *Nat. Phys.* **10**, 39 (2014).

[S30] X Mao, TC Lubensky, Maxwell lattices and topological mechanics. *Annu. Rev. Condens. Matter Phys.* **9**, 413–433 (2018).

[S31] LD Landau, EM Lifshitz, *Quantum mechanics: non-relativistic theory*. (Elsevier) Vol. 3, (2013).

[S32] S Ryu, AP Schnyder, A Furusaki, AW Ludwig, Topological insulators and superconductors: tenfold way and dimensional hierarchy. *New J. Phys.* **12**, 065010 (2010).

[S33] CK Chiu, JC Teo, AP Schnyder, S Ryu, Classification of topological quantum matter with symmetries. *Rev. Mod. Phys.* **88**, 035005 (2016).

[S34] W Su, J Schrieffer, AJ Heeger, Solitons in polyacetylene. *Phys. review letters* **42**, 1698 (1979).

[S35] T Lubensky, C Kane, X Mao, A Souslov, K Sun, Phonons and elasticity in critically coordinated lattices. *Reports on Prog. Phys.* **78**, 073901 (2015).

[S36] BA Bernevig, TL Hughes, *Topological insulators and topological superconductors*. (Princeton university press), (2013).

[S37] RD Kamien, The geometry of soft materials: a primer. *Rev. Mod. physics* **74**, 953 (2002).

[S38] L Fu, CL Kane, Topological insulators with inversion symmetry. *Phys. Rev. B* **76**, 045302 (2007).

[S39] TL Hughes, E Prodan, BA Bernevig, Inversion-symmetric topological insulators. *Phys. Rev. B* **83**, 245132 (2011).

[S40] M Sato, Topological odd-parity superconductors. *Phys. Rev. B* **81**, 220504 (2010).

[S41] L Fu, Topological crystalline insulators. *Phys. Rev. Lett.* **106**, 106802 (2011).

[S42] Y Ando, L Fu, Topological crystalline insulators and topological superconductors: from concepts to materials. *Annu. Rev. Condens. Matter Phys.* **6**, 361–381 (2015).
[S43] MZ Hasan, CL Kane, Colloquium: topological insulators. *Rev. modern physics* **82**, 3045 (2010).
[S44] G Bal, Topological invariants for interface modes. *arXiv preprint arXiv:1906.08345* (2019).
[S45] S Shankar, MJ Bowick, MC Marchetti, Topological sound and flocking on curved surfaces. *Phys. Rev. X* **7**, 031039 (2017).
[S46] P Delplace, J Marston, A Venaille, Topological origin of equatorial waves. *Science* **358**, 1075–1077 (2017).
[S47] A Souslov, K Dasbiswas, M Fruchart, S Vaikuntanathan, V Vitelli, Topological waves in fluids with odd viscosity. *Phys. review letters* **122**, 128001 (2019).
[S48] S Shankar, A Souslov, MJ Bowick, MC Marchetti, V Vitelli, Topological active matter. *arXiv preprint arXiv:2010.00364* (2020).
[S49] BGg Chen, N Upadhyaya, V Vitelli, Nonlinear conduction via solitons in a topological mechanical insulator. *Proc. Natl. Acad. Sci.* **111**, 13004–13009 (2014).
[S50] A Košmrlj, DR Nelson, Statistical mechanics of thin spherical shells. *Phys. Rev. X* **7**, 011002 (2017).
[S51] D Nelson, T Piran, S Weinberg, *Statistical mechanics of membranes and surfaces.* (World Scientific), (2004).